New physics analysis of baryonic Λ_b decays with dileptons or dineutrinos in the final state within the SMEFT framework

Nilakshi Das[*] and Rupak Dutta[†]
National Institute of Technology Silchar, Silchar 788010, India

(Received 27 July 2023; accepted 1 November 2023; published 30 November 2023)

The dileptons and dineutrinos observed in the final states of flavor-changing neutral b decays provide an ideal platform for probing physics beyond the standard model. Although the latest measurements of $R_{K^{(*)}}$ agree well with the standard model prediction, there exists several other observables such as P_5', $\mathcal{B}(B_s \to \phi\mu^+\mu^-)$ and $\mathcal{B}(B_s \to \mu^+\mu^-)$ in $b \to s\ell^+\ell^-$ transition decays that shows deviation from the standard model prediction. Similarly, very recently Belle II collaboration reported a more precise upper bound of $\mathcal{B}(B \to K^+\nu\bar{\nu}) < 4.1 \times 10^{-5}$ by employing a new inclusive tagging approach and it also deviates from the standard model expectation. The $b \to s\ell^+\ell^-$ and $b \to s\nu\bar{\nu}$ transition decays are related not only in the standard model but also in beyond the standard model physics due to $SU(2)_L$ gauge symmetry, and can be most effectively investigated using the standard model effective field theory formalism. Additionally, the $b \to s\nu\bar{\nu}$ decay channels are theoretically cleaner than the corresponding $b \to s\ell^+\ell^-$ decays, as these processes do not get contributions from nonfactorizable corrections and photonic penguin contributions. In this context, we study $\Lambda_b \to (\Lambda^*(\to pK^-), \Lambda(\to p\pi))(\mu^+\mu^-, \nu\bar{\nu})$ baryonic decays undergoing $b \to s\ell^+\ell^-$ and $b \to s\nu\bar{\nu}$ quark level transitions in a standard model effective field theory formalism. We give predictions of several observables pertaining to these decay channels in the standard model and in case of several new physics scenarios.

DOI: 10.1103/PhysRevD.108.095051

I. INTRODUCTION

In high-energy physics experiments, such as those at particle accelerators, it is possible to produce and detect intermediate states of quantum particles that have much greater mass than the initial and final particles. These intermediate states are often short-lived and can only be observed through the detection of their decay products. In this context, study of flavor changing charged current (FCCC) and neutral current (FCNC) transitions of b hadrons is crucial as they can provide important information regarding such intermediate quantum states. Moreover, FCNC transition decays are, in principle, more sensitive to various new physics (NP) effects as they proceed either via loop level or box level diagrams where the intervention of heavier particles comes into the picture. Hence, study of these decays would offer a powerful tool to search for NP that lies beyond the standard model (SM). Over the past several years, the FCNC B decays have been the center of attention of the particle physics community especially due to discrepancies observed at *BABAR*, Belle, and more recently at LHCb. The measured values of the lepton flavor sensitive observable such as the ratio of branching fractions R_K and R_{K^*} in $B \to K^{(*)}\ell^+\ell^-$ ($\ell \in e, \mu$) decays deviate from the SM prediction. These discrepancies hint for a possible violation of lepton flavor universality (LFU) in $b \to s\ell^+\ell^-$ transition decays.

Earlier LHCb measurement of R_K in $q^2 \in [1.1, 6.0]$ GeV^2 showed 3.1σ deviation from the SM expectation [1]. Similarly, earlier measurements of R_{K^*} from both LHCb [2,3] and Belle [4] in $q^2 \in [0.045, 1.1]$ and $q^2 \in [1.1, 6.0]$ GeV^2 bins showed 2.2–2.5σ deviation [5,6] from SM. However, very recent LHCb results [7,8], announced in December 2022, has completely changed the entire scenario. The latest measured values of $R_K = 0.994^{+0.090}_{-0.082}$ (stat)$^{+0.027}_{-0.029}$(syst) and $R_{K^*} = 0.927^{+0.093}_{-0.087}$(stat)$^{+0.034}_{-0.033}$(syst) in $q^2 \in [0.045, 1.1]$ GeV^2 and $R_K = 0.949^{+0.042}_{-0.041}$ (stat)$^{+0.023}_{-0.023}$(syst) and $R_{K^*} = 1.027^{+0.072}_{-0.068}$(stat)$^{+0.027}_{-0.027}$(syst) in $q^2 \in [1.1, 6.0]$ GeV^2 show an overall agreement with the SM prediction with 0.2 standard deviation [7,8].

Although R_K and R_{K^*} seem to be SM like, the possibilities of NP cannot be completely ruled out. Apart from R_K and R_{K^*}, there are several other observables where the discrepancy between the measured value and the SM prediction still exists. Measurement of P_5' from

[*]nilakshi_rs@phy.nits.ac.in
[†]rupak@phy.nits.ac.in

LHCb [9,10] and ATLAS [11] show 3.3σ deviation from the SM prediction. Similarly, CMS [12] and Belle [13] measurements show 1σ and 2.6σ deviations, respectively [14–16]. Again, the measured value of the branching fraction of $B_s \to \phi\mu^+\mu^-$ in $q^2 \in [1.1, 6.0]$ GeV^2 deviates from the SM prediction at 3.3σ [17–19]. Moreover, measurements of the ratio of branching ratio [20] $R_{K_s^0}$ and $R_{K^{*+}}$, isospin partners of R_K and R_{K^*}, also deviate from the SM prediction at 1.4σ and 1.5σ, respectively.

There exists another class of FCNC transition decays with neutral leptons in the final state that are mediated via $b \to s\nu\bar{\nu}$ quark level transitions. Theoretically these dineutrino channels are clean as they do not suffer from hadronic uncertainties beyond the form factors such as the nonfactorizable corrections and photon penguin contributions. However, they are very challenging from the experimental point of view due to the presence of neutrinos in the final state. In spite of that, *BABAR*, Bell/Belle II have managed to provide the upper bounds of $B \to K^{(*)}\nu\bar{\nu}$ decays to be $\mathcal{B}(B^+ \to K^+\nu\bar{\nu}) \leq 4.1 \times 10^{-5}$ [21] and $\mathcal{B}(B^0 \to K^{0*}\nu\bar{\nu}) \leq 1.8 \times 10^{-5}$, respectively. Combined with the previous measurements from Belle and *BABAR* one estimates the world average value of the branching fraction to be $\mathcal{B}(B^+ \to K^+\nu\bar{\nu}) \leq (1.1 \pm 04) \times 10^{-5}$ [21]. A combined analysis of $b \to s\ell^+\ell^-$ and $b \to s\nu\bar{\nu}$ decays is theoretically well motivated as these two channels are closely related not only in the SM but also in beyond the SM under $SU(2)_L$ gauge symmetry. Moreover, a more precise measurements of $B \to K^{(*)}\nu\bar{\nu}$ branching fraction in future may provide useful insight into NP that may be present in $b \to s\ell^+\ell^-$ transition decays.

Various analyses, both model-dependent and model-independent, have been performed to account for these anomalies. A nonexhaustive compilation of relevant literature can be found in the Refs. [22–40]. To confirm the presence of NP, we need to perform measurements of similar observables in different decay processes that proceed via same quark level transitions. Similarly, it is very important to perform a detailed angular analysis in order to look for several form factor independent angular observables which are sensitive to NP. In this context, baryonic $\Lambda_b^0 \to \Lambda^{(*)}(\to pK^-, p\pi)\mu^+\mu^-$ decay mode has got lot of attention. The recent measurement from LHCb suggests that although the ratio R_{pK} is compatible with SM, there is suppression in $\mathcal{B}(\Lambda_b \to pK\mu^+\mu^-)$ compared to $\mathcal{B}(\Lambda_b \to pKe^+e^-)$ [41]. To interpret this result, it is essential to have a precise theoretical knowledge of various excited states of Λ baryon contributing to pK region. The Λ_b decay to $\Lambda^* \equiv \Lambda^*(1520)$ has the largest contribution among the various semileptonic modes of Λ_b decays to hadrons. Due to its spin parity of $J^P = 3/2^-$ and strong decay into the $N\bar{K}$ pair, the Λ^* is readily distinguishable from nearby hadrons, including the $\Lambda(1600)$, $\Lambda(1405)$, and weakly decaying $\Lambda(1116)$, which have a spin parity of $J^P = 1/2^\pm$. In Refs. [42,43], the authors calculate the LQCD form factors in the weak transition of $\Lambda_b \to \Lambda(1520)$ decay, while in Refs. [44,45], the authors performed angular analyses of $\Lambda_b \to \Lambda\ell^+\ell^-$ decays for massless and massive leptons, respectively. Additionally, in Ref. [46], the authors investigated the angular distributions of $\Lambda_b \to \Lambda(1520)\ell^+\ell^-$ and discussed the potential for identifying NP effects. Similarly, the authors in Ref. [47] study the $\Lambda_b \to \Lambda(1520)(\to N\bar{K})\ell^+\ell^-$ process with $N\bar{K} = \{pK^-, n\bar{K}^0\}$ and examine several angular observables. The study is performed with a set of operators where the SM operator basis is supplemented with its chirality flipped counterparts and new scalar and pseudoscalar operators. The three-body light-front quark model based on the gaussian expansion method is used to systematically investigate the $\Lambda_b \to \Lambda(1520)(\to N\bar{K})\ell^+\ell^-$ ($\ell = e, \mu, \tau$) decay process. Several theoretical methods, such as lattice QCD (LQCD) [48,49], QCD sum rules (QCDSR) [50], light-cone sum rule (LCSR) [51–55], covariant quark model (CQM) [56], nonrelativistic quark model [57], and Bethe-Salpeter approach [58], have been used to study the rare decay $\Lambda_b \to \Lambda\ell^+\ell^-$. The initial measurement of the decay was conducted by the CDF Collaboration [59], followed by a subsequent measurement by the LHCb Collaboration [60,61]. In Ref. [62] QCD sum rules were used to calculate the $\Lambda_b \to \Lambda$ transition form factors and to study the unpolarized decay. The form factors for $\Lambda_b \to \Lambda$ at large recoil were analyzed using a sum-rule approach to study spectator-scattering corrections [63]. Light-cone distribution amplitude of Λ_b wave function was studied in [64–66] to further understand the theoretical aspects. A model-independent analysis for unpolarized $\Lambda_b \to \Lambda \times (\to N\pi)\ell^+\ell^-$ decay was performed in [45,67–70] using a complete set of dimension-six operators. The angular distribution of the decay with unpolarized Λ_b baryon has been explored in Refs. [70,71], while in Ref. [72], the study involved polarized Λ_b baryon. Furthermore, in Ref. [73], the $b \to s\mu^+\mu^-$ Wilson coefficients were examined by utilizing the complete angular distribution of the rare decay $\Lambda_b \to \Lambda(\to p\pi)\mu^+\mu^-$ measured by the LHCb Collaboration [61]. Similarly, in Ref. [74], the authors calculate the branching fraction of $\Lambda_b \to \Lambda\nu\bar{\nu}$ decay by taking the polarized Λ_b and Λ. Moreover, in Ref. [75], the authors analyse $\Lambda_b \to \Lambda\nu\bar{\nu}$ decay by considering the Z' model. Here the authors calculate the branching ratio as well as the longitudinal, transversal and normal polarizations of the dineutrino decay channel of the baryonic decay $\Lambda_b \to \Lambda$ within the SM as well as in the presence of leptophobic Z' model.

In this paper, we study the implication of $b \to s\ell^+\ell^-$ anomalies on $\Lambda_b \to (\Lambda^*(\to pK^-), \Lambda(\to p\pi))\mu^+\mu^-$ and $\Lambda_b \to (\Lambda^*(\to pK^-), \Lambda(\to p\pi))\nu\bar{\nu}$ decays in a model independent way. Our work differs significantly from others. For NP analysis, we construct several $1D$ and $2D$ NP scenarios emerging out of dimension six operators in the standard model effective field theory (SMEFT) formalism.

We obtain the allowed NP parameter space by performing a global fit to the $b \to s\ell^+\ell^-$ data. Moreover, we also use the measured upper bound on $\mathcal{B}(B \to K^{(*)}\nu\bar{\nu})$ to check the compatibility of our fit results.

The paper is organized as follows. In Sec. II, we start with a brief description of the SMEFT framework and write down the effective Hamiltonian for the $b \to s\nu\bar{\nu}$ and $b \to s\ell^+\ell^-$ quark level transition decays. Subsequently, we report all the relevant formulas for the observables in Sec. II. In Sec. III, we first report all the input parameters that are used for our analysis. A detailed discussion of the results pertaining to $\Lambda_b \to (\Lambda^*(\to pK^-), \Lambda(\to p\pi))\mu^+\mu^-$ and $\Lambda_b \to (\Lambda^*(\to pK^-), \Lambda(\to p\pi))\nu\bar{\nu}$ baryonic decay observables in the SM and in case of NP scenarios are also presented. Finally, we conclude with a brief summary of our results in Sec. IV.

II. THEORY

To date, no direct evidence of new particles near the electroweak scale has been observed from searches conducted in the Large Hadron Collider (LHC). Nevertheless, these searches provide indirect evidence supporting the existence of NP at a scale beyond the electroweak scale. To explore indirect signatures of NP in a model-independent way, the SMEFT framework offers a more efficient approach. The SMEFT Lagrangian explains particle interactions in the SM and in all possible extensions of SM. It is constructed by incorporating higher-dimensional operators into the SM Lagrangian while maintaining the $SU(3)_C \times SU(2)_L \times U(1)_Y$ gauge symmetry. These higher-dimensional operators are suppressed by a factor that depends on a new energy scale. The SMEFT Lagrangian comprises all sets of these higher-dimensional operators that are consistent with the underlying gauge symmetry. For investigating NP beyond the SM at low energies, this framework provides an excellent platform. From the fundamental aspect of the electroweak theory, the left-handed charged leptons are related to neutral leptons through the $SU(2)_L$ symmetry. In this study, we concentrate on the connection between $b \to s\ell^+\ell^-$ and $b \to s\nu\bar{\nu}$ transition decays within the SMEFT framework by considering dimension six operators. If no new particles are observed at the LHC, it will imply a NP scale that is greater than the energy scale of the LHC. The SMEFT analysis would be crucial in this situation as it offers a way to examine the implications of NP indirectly by evaluating their effects on SM low energy processes.

The effective Lagrangian corresponding to dimension six operators is expressed as [76]

$$\mathcal{L}^{(6)} = \sum_i \frac{c_i}{\Lambda^2} \mathcal{Q}_i. \tag{1}$$

Among all the operators, the relevant operators contributing to both $b \to s\nu\bar{\nu}$ and $b \to s\ell^+\ell^-$ decays are

$$\begin{aligned} &\mathcal{Q}_{Hq}^{(1)} = i(\bar{q}_L\gamma_\mu q_L)H^\dagger D^\mu H, \qquad \mathcal{Q}_{Hq}^{(3)} = i(\bar{q}_L\gamma_\mu \tau^a q_L)H^\dagger D^\mu \tau_a H, \qquad \mathcal{Q}_{Hd} = i(\bar{d}_R\gamma_\mu d_R)H^\dagger D^\mu H, \\ &\mathcal{Q}_{ql}^{(1)} = (\bar{q}_L\gamma_\mu q_L)(\bar{l}_L\gamma^\mu l_L), \qquad \mathcal{Q}_{ql}^{(3)} = (\bar{q}_L\gamma_\mu \tau^a q_L)(\bar{l}_L\gamma^\mu \tau_a l_L), \qquad \mathcal{Q}_{dl} = (\bar{d}_R\gamma_\mu d_R)(\bar{l}_L\gamma^\mu l_L). \end{aligned} \tag{2}$$

Similarly, the operators contributing only to $b \to s\ell^+\ell^-$ decays are

$$\mathcal{Q}_{de} = (\bar{d}_R\gamma_\mu d_R)(\bar{e}_R\gamma^\mu e_R), \qquad \mathcal{Q}_{qe} = (\bar{q}_L\gamma_\mu q_L)(\bar{e}_R\gamma^\mu e_R). \tag{3}$$

Here, $\mathcal{Q}_{Hq}^{(1)}$, $\mathcal{Q}_{Hq}^{(3)}$, and $\mathcal{Q}_{Hd}$ are the Higgs-quark operators, with "H" representing the Higgs doublet. The term τ_a signifies the $SU(2)$ Pauli matrices and D^μ represents the covariant derivative. Furthermore, $\mathcal{Q}_{ql}^{(1)}$, $\mathcal{Q}_{ql}^{(3)}$, $\mathcal{Q}_{dl}$, $\mathcal{Q}_{de}$, and $\mathcal{Q}_{qe}$ are the four-fermion operators. Here, q and l represent the quark and lepton $SU(2)_L$ doublets, respectively, while d and e correspond to the weak singlet states of down type quarks and leptons.

At low energy, the most general $\Delta F = 1$ effective Hamiltonian governing both $b \to s\nu\bar{\nu}$ and $b \to s\ell^+\ell^-$ decays can be written as [35,77],

$$\mathcal{H}_{\text{eff}} = -\frac{4G_F}{\sqrt{2}} V_{tb}V_{ts}^* \frac{e^2}{16\pi^2} \sum_i C_i \mathcal{O}_i + \text{H.c.}, \tag{4}$$

where G_F is the Fermi coupling constant, $|V_{tb}V_{ts}^*|$ are the associated Cabibbo-Kobayashi-Maskawa (CKM) matrix elements. The sum $i = L, R$ comprises the operators $\mathcal{O}_{L,R}$ with the corresponding WCs $C_{L,R}$ contributing to $b \to s\nu\bar{\nu}$ decays. They are

$$\begin{aligned} \mathcal{O}_L &= (\bar{s}\gamma_\mu P_L b)(\bar{\nu}\gamma^\mu(1-\gamma_5)\nu), \\ \mathcal{O}_R &= (\bar{s}\gamma_\mu P_R b)(\bar{\nu}\gamma^\mu(1-\gamma_5)\nu). \end{aligned} \tag{5}$$

Here, $P_{L,R} = (1 \mp \gamma_5)/2$ represents the projection operator. In the SM, $C_R^{\text{SM}} = 0$ and the value of C_L^{SM} is calculated to be

$$C_L^{\text{SM}} = -X_t/s_w^2 = -6.38 \pm 0.06, \qquad X_t = 1.469 \pm 0.017, \qquad s_w^2 = 0.23126(5). \tag{6}$$

Similarly, for $i = 9^{(\prime)}, 10^{(\prime)}$, the sum comprises the operators $\mathcal{O}_{9^{(\prime)},10^{(\prime)}}$ with the corresponding WCs $C_{9^{(\prime)},10^{(\prime)}}$ that contribute to $b \to s\ell^+\ell^-$ decays. The operators are

$$\mathcal{O}_9^{(\prime)} = (\bar{s}\gamma_\mu P_{L(R)} b)(\bar{l}\gamma^\mu l), \qquad \mathcal{O}_{10}^{(\prime)} = (\bar{s}\gamma_\mu P_{L(R)} b)(\bar{l}\gamma^\mu \gamma_5 l). \tag{7}$$

In the presence of dimension six SMEFT operators, the WCs $C_{9,10,L}$ and $C_{9',10',R}$ get modified. They can be expressed as follows [77]

$$\begin{aligned} C_9 &= C_9^{\rm SM} + \tilde{c}_{qe} + \tilde{c}_{ql}^{(1)} + \tilde{c}_{ql}^{(3)} - \zeta \tilde{c}_Z \\ C_{10} &= C_{10}^{\rm SM} + \tilde{c}_{qe} - \tilde{c}_{ql}^{(1)} - \tilde{c}_{ql}^{(3)} + \tilde{c}_Z \\ C_L^\nu &= C_L^{\rm SM} + \tilde{c}_{ql}^{(1)} - \tilde{c}_{ql}^{(3)} + \tilde{c}_Z \\ C_9' &= \tilde{c}_{de} + \tilde{c}_{dl} - \zeta \tilde{c}_Z' \\ C_{10}' &= \tilde{c}_{de} - \tilde{c}_{dl} + \tilde{c}_Z' \\ C_R^\nu &= \tilde{c}_{dl} + \tilde{c}_Z', \end{aligned} \tag{8}$$

where, $\tilde{c}_Z = \frac{1}{2}(\tilde{c}_{Hq}^{(1)} + \tilde{c}_{Hq}^{(3)})$, $\tilde{c}_Z' = \frac{1}{2}(\tilde{c}_{Hd})$ and $\zeta \approx 0.08$ represents the small vector coupling to charged leptons.

It should be noted that we have not included the long distance contributions coming from $c\bar{c}$ resonant states in our analysis. It is shown in Refs. [78–81] that the nonlocal effects are, in fact, very important even below the charmonium contribution. In $q^2 \in (1,4)$ GeV^2, the charm loop corrections to C_9 is estimated to be around 20% and 5% for the $B \to K^* \ell^+ \ell^-$ and $B \to K \ell^+ \ell^-$ decays, respectively. These nonfactorizable contributions significantly affect the differential width and the forward-backward asymmetry in $B \to K^* \ell^+ \ell^-$ decays. Similarly, in Refs. [40,81], the authors have carried out the first global analysis of nonlocal contributions in $B \to K^* \ell^+ \ell^-$ and $B_s \to \phi \ell^+ \ell^-$ decays. They obtain SM predictions for these decays in the $0 < q^2 < M_{J/\psi}$ region by using a modified analytic parametrization of nonlocal matrix elements. The results agree quite well with the results obtained using QCD factorization approach. The uncertainties, however, are substantially larger. Since most theoretical papers addressing LFU violation in $b \to s \ell^+ \ell^-$ decays neglect the hadronic nonlocal effects, we exclude these corrections in our current analysis.

A. Differential decay distribution and q^2 dependent observables for $\Lambda_b \to \Lambda^* (\to pK^-) \ell^+ \ell^-$ decays

The four-fold angular distribution for $\Lambda_b \to \Lambda^* (\to pK^-) \ell^+ \ell^-$ decay can be expressed as [45]

$$\begin{aligned} \frac{d^4\mathcal{B}}{dq^2 d\cos\theta_\ell d\cos\theta_{\Lambda^*} d\phi} = \frac{3}{8\pi} \Big[& \Big(K_{1c}\cos\theta_\ell + K_{1cc}\cos^2\theta_\ell + K_{1ss}\sin^2\theta_\ell\Big)\cos^2\theta_{\Lambda^*} \\ & + \Big(K_{2c}\cos\theta_\ell + K_{2cc}\cos^2\theta_\ell + K_{2ss}\sin^2\theta_\ell\Big)\sin^2\theta_{\Lambda^*} \\ & + \Big(K_{3ss}\sin^2\theta_\ell\Big)\sin^2\theta_{\Lambda^*}\cos\phi + \Big(K_{4ss}\sin^2\theta_\ell\Big)\sin^2\theta_{\Lambda^*}\sin\phi\cos\phi \\ & + \Big(K_{5s}\sin\theta_\ell + K_{5sc}\sin\theta_\ell\cos\theta_\ell\Big)\sin\theta_{\Lambda^*}\cos\theta_{\Lambda^*}\cos\phi \\ & + \Big(K_{6s}\sin\theta_\ell + K_{6sc}\sin\theta_\ell\cos\theta_\ell\Big)\sin\theta_{\Lambda^*}\cos\theta_{\Lambda^*}\sin\phi\Big], \end{aligned} \tag{9}$$

where θ_{Λ^*} represents the angle formed by the proton with the daughter baryon Λ^* in the rest frame of Λ_b. Similarly, in the rest frame of the lepton pair, θ_ℓ denotes the angle formed by the ℓ^- with respect to the direction of the daughter baryon Λ^*. Moreover, in the rest frame of Λ_b, ϕ defines the angle between the planes containing pK^- and the lepton pair. The angular coefficients $K_{\{...\}}$, $\{\cdots\} = 1c, \cdots 6sc$, can be expressed as

$$K_{\{...\}} = K_{\{...\}} + \frac{m_\ell}{\sqrt{q^2}} K'_{\{...\}} + \frac{m_\ell^2}{q^2} K''_{\{...\}} \tag{10}$$

Here the first term K corresponds to massless leptons, whereas, K' and K'' correspond to linear $[\mathcal{O}(m_\ell/\sqrt{q^2})]$ and quadratic $[\mathcal{O}(m_\ell^2/q^2)]$ mass corrections, respectively. The explicit expressions for $K_{\{...\}}$, $K'_{\{...\}}$ and $K''_{\{...\}}$ in terms of transversely amplitude are taken Ref. [45].

From the differential decay distributions, one can construct several physical observables.

(i) The differential branching ratio $d\mathcal{B}/dq^2$, the lepton forward-backward asymmetry $A_{\rm FB}(q^2)$, the fraction of longitudinal polarization $F_L(q^2)$ and the ratio of branching fraction $R_{\Lambda^*}(q^2)$ are defined as

$$\begin{aligned} &\frac{d\mathcal{B}}{dq^2} = \frac{1}{3}\Big[K_{1cc} + 2K_{1ss} + 2K_{2cc} + 4K_{2ss} + 2K_{3ss}\Big], \qquad F_L = 1 - \frac{2(K_{1cc} + 2K_{2cc})}{K_{1cc} + 2(K_{1ss} + K_{2cc} + 2K_{2ss} + K_{3ss})} \\ &A_{\rm FB} = \frac{3(K_{1c} + 2K_{2c})}{2[K_{1cc} + 2(K_{1ss} + K_{2cc} + 2K_{2ss} + K_{3ss})]}, \qquad R_{\Lambda^*}(q^2) = \frac{d\mathcal{B}/dq^2|_{\mu-{\rm mode}}}{d\mathcal{B}/dq^2|_{e-{\rm mode}}}. \end{aligned} \tag{11}$$

(ii) We define several angular observables such as $\hat{K}_{1c}$, $\hat{K}_{1cc}$, $\hat{K}_{1ss}$, $\hat{K}_{2c}$, $\hat{K}_{2cc}$, $\hat{K}_{2ss}$, $\hat{K}_{3ss}$, $\hat{K}_{4ss}$, $\hat{K}_{4s}$, $\hat{K}_{5s}$. They are

$$\hat{K}_{1c} = \frac{K_{1c}}{d\mathcal{B}/dq^2}, \qquad \hat{K}_{1cc} = \frac{K_{1cc}}{d\mathcal{B}/dq^2}, \qquad \hat{K}_{1ss} = \frac{K_{1ss}}{d\mathcal{B}/dq^2}, \qquad \hat{K}_{2c} = \frac{K_{2c}}{d\mathcal{B}/dq^2}, \qquad \hat{K}_{2cc} = \frac{K_{2cc}}{d\mathcal{B}/dq^2}$$
$$\hat{K}_{2ss} = \frac{K_{2ss}}{d\mathcal{B}/dq^2}, \qquad \hat{K}_{3ss} = \frac{K_{3ss}}{d\mathcal{B}/dq^2}, \qquad \hat{K}_{4ss} = \frac{K_{4ss}}{d\mathcal{B}/dq^2}, \qquad \hat{K}_{5s} = \frac{K_{5s}}{d\mathcal{B}/dq^2}. \tag{12}$$

It is important to note that the angular coefficients ($\hat{K}_{1c}$, $\hat{K}_{2c}$), ($\hat{K}_{1cc}$, $\hat{K}_{2cc}$), and ($\hat{K}_{1ss}$, $\hat{K}_{2ss}$) exhibit a strict relation in the SM. That is

$$\frac{\hat{K}_{1c}}{\hat{K}_{2c}} = 4, \qquad \frac{\hat{K}_{1cc}}{\hat{K}_{2cc}} = 4, \qquad \frac{\hat{K}_{1ss}}{\hat{K}_{2ss}} = 4. \tag{13}$$

B. Differential decay distribution and q^2 dependent observables for $\Lambda_b \to \Lambda(\to p\pi)\ell^+\ell^-$

The four fold angular distribution for $\Lambda_b \to \Lambda(\to p\pi)\ell^+\ell^-$ is defined as [68]

$$\begin{aligned}\frac{d^4\mathcal{B}}{dq^2 d\cos\theta_\ell d\cos\theta_\Lambda d\phi} = \frac{3}{8\pi}&(K_{1ss}\sin^2\theta_\ell + K_{1cc}\cos^2\theta_\ell + K_{1c}\cos\theta_\ell) \\ &+ (K_{2ss}\sin^2\theta_\ell + K_{2cc}\cos^2\theta_\ell + K_{2c}\cos\theta_\ell)\cos\theta_\Lambda \\ &+ (K_{3sc}\sin\theta_\ell\cos\theta_\ell + K_{3s}\sin\theta_\ell)\sin\theta_\Lambda\sin\phi \\ &+ (K_{4sc}\sin\theta_\ell\cos\theta_\ell + K_{3s}\sin\theta_\ell)\sin\theta_\Lambda\cos\phi,\end{aligned} \tag{14}$$

where the angular coefficients K_{ijk} can be expressed as

$$K_{ijk} = K_{ijk} + \frac{m_\ell}{\sqrt{q^2}}K'_{ijk} + \frac{m_\ell^2}{q^2}K''_{ijk}, \tag{15}$$

with $ijk = 1ss \cdots 4s$. The explicit expressions for K, K', and K'' are taken from Ref. [68].

We define several physical observables pertaining to this decay mode.

(i) Differential branching ratio $d\mathcal{B}/dq^2$, the lepton forward-backward asymmetry $A^l_{\rm FB}(q^2)$, the fraction of longitudinal polarization $F_L(q^2)$ and the ratio of branching fraction $R_\Lambda(q^2)$ are defined as

$$\frac{d\mathcal{B}}{dq^2} = 2K_{1ss} + K_{1cc}, \qquad F_L = \frac{2K_{1ss} - K_{1cc}}{2K_{1ss} + K_{1cc}}, \qquad A_{\rm FB} = \frac{3}{2}\frac{K_{1c}}{2K_{1ss} + K_{1cc}}, \qquad R_\Lambda(q^2) = \frac{d\mathcal{B}/dq^2|_{\mu-\rm mode}}{d\mathcal{B}/dq^2|_{e-\rm mode}}. \tag{16}$$

(ii) Angular observables such as $\hat{K}_{1c}$, $\hat{K}_{1cc}$, $\hat{K}_{1ss}$, $\hat{K}_{2c}$, $\hat{K}_{2cc}$, $\hat{K}_{2ss}$, $\hat{K}_{3ss}$, $\hat{K}_{3sc}$, $\hat{K}_{4sc}$, $\hat{K}_{4s}$ are defined as

$$\hat{K}_{1c} = \frac{K_{1c}}{d\mathcal{B}/dq^2}, \qquad \hat{K}_{1cc} = \frac{K_{1cc}}{d\mathcal{B}/dq^2}, \qquad \hat{K}_{1ss} = \frac{K_{1ss}}{d\mathcal{B}/dq^2}, \qquad \hat{K}_{2c} = \frac{K_{2c}}{d\mathcal{B}/dq^2}, \qquad \hat{K}_{2cc} = \frac{K_{2cc}}{d\mathcal{B}/dq^2}$$
$$\hat{K}_{2ss} = \frac{K_{2ss}}{d\mathcal{B}/dq^2}, \qquad \hat{K}_{3sc} = \frac{K_{3sc}}{d\mathcal{B}/dq^2}, \qquad \hat{K}_{3s} = \frac{K_{3s}}{d\mathcal{B}/dq^2}, \qquad \hat{K}_{4sc} = \frac{K_{4sc}}{d\mathcal{B}/dq^2}, \qquad \hat{K}_{4s} = \frac{K_{4s}}{d\mathcal{B}/dq^2}. \tag{17}$$

All the relevant expressions for $\Lambda_b \to \Lambda^*(\to pK^-)\nu\bar{\nu}$ and $\Lambda_b \to \Lambda(\to p\pi)\nu\bar{\nu}$ decays are written in the Appendix.

III. RESULTS

A. Input parameters

The numerical values of all the input parameters used in the paper are summarized in the Table I. Input parameters, such as the masses of mesons and quarks are expressed in GeV units, the Fermi coupling constant G_F is in GeV^{-2} units and the life time of Λ_b baryon is in seconds.

TABLE I. Input parameters [45,68,82].

Parameter	Value	Parameter	Value	Parameter	Value	Parameter	Value	Parameter	Value
m_e	0.000511	m_μ	0.105658	$\alpha_e(m_b)$	1/127.925(16)	$\lvert V_{tb}V_{ts}^*\rvert$	0.0401 ± 0.0010	$m_c(\overline{\mathrm{MS}})$	1.28 GeV
m_{Λ_b}	5.619 GeV	μ_b	4.8	m_{Λ^*}	1.115	τ_{Λ_b}	$(1.470 \pm 0.010) \times 10^{-12}$	m_{Λ_b}	5.619 GeV
$m_b^{\overline{\mathrm{MS}}}$	4.2	$m_c^{\overline{\mathrm{MS}}}$	1.28	m_b^{pole}	4.8	m_{Λ^*}	1.115	$\mathcal{B}_{\Lambda^*}$	0.45 ± 0.01
$\mathcal{B}_\Lambda$	0.642 ± 0.013	α_Λ	0.443	$\alpha_{\Lambda'}$	0.333				

For hadronic inputs such as $\Lambda_b \to \Lambda^*$ form factors, we use the values reported in Ref. [57], and for $\Lambda_b \to \Lambda$ form factors, we use the LQCD results of Ref. [49]. In case of $\Lambda_b \to \Lambda^*$ decay, the available data for the LQCD form factor only reach down to approximately 16.3 GeV^2, and the accuracy of the form factor's parameterization is not reliable for lower values of q^2. It should be noted that using the LQCD form factor, dB/dq^2 is found to be lower by a factor of 2 than the value predicted using the MCN form factors [57]. Also by taking LQCD form factors, the angular observables are qualitatively similar to those computed using the MCN form factors [57]. This information is explicitly mentioned in the Refs. [42,43]. In our analysis, we examine both $\Lambda_b \to \Lambda^*(1520)\ell^+\ell^-$ and $\Lambda_b \to \Lambda^*(1520)\nu\bar{\nu}$ decay channels using MCN form factors. Hence, by utilizing the MCN form factor, we ensure consistency while calculating the dB/dq^2 for the dineutrino channel in the entire q^2 range.

The relevant formula for the $\Lambda_b \to \Lambda^*$ form factors pertinent for our discussion is as follows [57]

$$F(\hat{s}) = (a_0 + a_2 p_\Lambda^2 + a_4 p_\Lambda^4) \exp\left(-\frac{3m_q^2}{2\tilde{m}_\Lambda^2}\frac{p_\Lambda^2}{\alpha_{\Lambda\Lambda'}^2}\right), \quad (18)$$

where

$$p_\Lambda = \frac{m_{\Lambda b}}{2}\sqrt{\phi(\hat{s})}, \quad \phi(\hat{s}) = (1-r)^2 - 2(1+r)\hat{s} + \hat{s}^2,$$
$$\alpha_{\Lambda\Lambda'} = \sqrt{\frac{\alpha_\Lambda^2 + \alpha_{\Lambda'}^2}{2}}. \quad (19)$$

Here $r = m_{\Lambda^*}^2/m_{\Lambda_b}^2$ and $\hat{s} \equiv q^2/m_{\Lambda b}^2$. We consider 5% uncertainty in the input parameters $F_i \in (i = 1\ldots4)$, $G_i \in (i = 1\ldots4)$, and $H_i(i = 1\ldots6)$. The values of these parameter, taken from Ref. [57], are reported in Table II.

Similarly, for $\Lambda_b \to \Lambda$ transition form factors, we use the relevant form factor formula from Ref. [49]. That is

$$f(q^2) = \frac{1}{1 - q^2/(m_{\mathrm{pole}}^f)^2}[a_0^f + a_1^f z(q^2, t_+)]. \quad (20)$$

To calculate the statistical uncertainties of the observable, we utilize the parameters from the "nominal" fit. However, to estimate the systematic uncertainties, we use a "higher-order" fit where the fit function is given by

$$f(q^2) = \frac{1}{1 - q^2/(m_{\mathrm{pole}}^f)^2}\left[a_0^f + a_1^f z(q^2, t_+) + a_2^f (z(q^2, t_+))^2\right]. \quad (21)$$

The function $z(q^2, t_+)$ is defined as

$$z(q^2, t_+) = \frac{\sqrt{t_+ - q^2} - \sqrt{t_+ - t_0}}{\sqrt{t_+ - q^2} + \sqrt{t_+ - t_0}}, \quad (22)$$

where $t_0 = (m_{\Lambda_b} - m_\Lambda)^2$ and $t_+ = (m_B + m_K)^2$. The fit parameters and masses used in our analysis are taken from Ref. [49]. For completeness, we report them in Table III.

B. SM predictions

In this section, we present the central values and the 1σ uncertainties of several observables for the $\Lambda_b \to \Lambda^*(\to pK^-)\ell^+\ell^-$ and $\Lambda_b \to \Lambda(\to p\pi)\ell^+\ell^-$ decay channels. More specifically, we give prediction of the branching ratio (BR), the ratio of branching ratios [$R_{\Lambda^{(*)}}$], the forward-backward asymmetry (A_{FB}), the longitudinal polarization fraction (F_L) for the $\mu^+\mu^-$ modes, respectively. We also report various angular observables such as $\hat{K}_{1ss}$, $\hat{K}_{2c}$, $\hat{K}_{2cc}$, $\hat{K}_{2ss}$, $\hat{K}_{3ss}$, $\hat{K}_{4ss}$, $\hat{K}_{4s}$, $\hat{K}_{5s}$ for $\Lambda_b \to \Lambda^*(\to pK^-)\ell^+\ell^-$ decay mode. Similarly, we report angular observables such as $\hat{K}_{1c}$, $\hat{K}_{1cc}$, $\hat{K}_{1ss}$, $\hat{K}_{2c}$, $\hat{K}_{2cc}$, $\hat{K}_{2ss}$, $\hat{K}_{3ss}$, $\hat{K}_{3sc}$, $\hat{K}_{4sc}$, $\hat{K}_{4s}$ for $\Lambda_b \to \Lambda(\to p\pi)\ell^+\ell^-$ decay mode as well. Moreover, we give predictions of several observables pertaining to $\Lambda_b \to \Lambda^*(\to pK^-)\nu\bar{\nu}$ and $\Lambda_b \to \Lambda(\to p\pi)\nu\bar{\nu}$ decay modes. The central values of the observables are obtained using the central values of the input parameters, whereas the uncertainties in each observable are determined by varying the uncertainties associated with inputs such as form factors and the CKM matrix elements within 1σ of their central values. For the $\mu^+\mu^-$ final states, we explore two q^2 bins, namely (1.1–6.0) and $(14.2 - q_{\mathrm{max}}^2)$ for the $\Lambda_b \to \Lambda^*(\to pK^-)\ell^+\ell^-$ decay mode and (1.1–6.0) and $(15.0 - q_{\mathrm{max}}^2)$ for the $\Lambda_b \to \Lambda(\to p\pi)\ell^+\ell^-$ decay mode, respectively. All the results are listed in Tables IV and V, respectively.

Our observations are as follows.

(i) The branching ratio of $\Lambda_b \to \Lambda^*(\to pK^-)\mu^+\mu^-$ mode is found to be of $\mathcal{O}(10^{-9})$, while the branching ratio of $\Lambda_b \to \Lambda(\to p\pi)\mu^+\mu^-$ decay mode is observed to be of $\mathcal{O}(10^{-7})$.

TABLE II. $\Lambda_b \to \Lambda^*$ form factor inputs [57].

$\Lambda^*(1520)$	F_1	F_2	F_3	F_4	G_1	G_2	G_3	G_4	H_1	H_2	H_3	H_4	H_5	H_6
a_0	−1.66	0.544	0.126	−0.0330	−0.964	0.625	−0.183	0.0530	−1.08	−0.507	0.187	0.0772	−0.0517	0.0206
a_2	−0.295	0.194	0.00799	−0.00977	−0.100	0.219	−0.0380	0.0161	−0.0732	−0.246	0.0295	0.0267	−0.0173	0.00679
a_4	0.00924	−0.00420	−0.000365	0.00211	0.00264	−0.00508	0.00351	−0.00221	0.00464	0.00309	−0.00107	−0.00217	0.00259	−0.000220

(ii) The values of F_L, $A_{\rm FB}$, $\hat{K}_{1c}$, $\hat{K}_{2c}$, $\hat{K}_{2ss}$, and $\hat{K}_{4ss}$ are observed to be lower at high q^2 bin compared to the values obtained in the low q^2 bin.

(iii) In the case of the $\Lambda_b \to \Lambda^*(\to pK^-)\mu^+\mu^-$ decay mode, values of $\hat{K}_{3s}$ and $\hat{K}_{4ss}$ are zero in the low q^2 bin, whereas they are nonzero in the high q^2 bin.

(iv) We found the ratios $\hat{K}_{1c}/\hat{K}_{2c}$, $\hat{K}_{1cc}/\hat{K}_{2cc}$, and $\hat{K}_{1ss}/\hat{K}_{2ss}$ to be equal to 4.

(v) As expected, value of $R_{\Lambda^{(*)}}$ is very close to unity.

(vi) The branching fraction of both $\Lambda_b \to \Lambda^*(\to pK^-)\nu\bar{\nu}$ and $\Lambda_b \to \Lambda(\to p\pi)\nu\bar{\nu}$ decay channels are found to be of $\mathcal{O}(10^{-6})$.

(vii) It is observed that the uncertainties in the dineutrino channels are less than the uncertainty in dilepton decay channels.

For completeness we also report the branching ratio for the $\Lambda_b \to \Lambda(\to p\pi)\tau^+\tau^-$ mode to be $(1.9 \pm 0.43) \times 10^{-7}$ in $q^2 \in [15.0 - q^2_{\rm max}]$ which is quite similar to the value reported in Ref. [68]. A slight difference is observed due to the different choice of input parameters.

The investigation of $b \to s\nu\bar{\nu}$ decays faces limitations at LHCb, primarily due to its challenges in detecting missing energy. However, there has been significant progress in this area, notably by the Belle-II collaboration [83], which recently presented the first experimental evidence for the $B^+ \to K^+\nu\bar{\nu}$ decay. The measured branching ratio $\mathcal{B}(B^+ \to K^+\nu\bar{\nu}) = (2.4 \pm 0.7) \times 10^{-5}$, exceeds the SM prediction by 2.8σ. Additionally, Belle-II is actively investigating $B^0 \to K^{*0}\nu\bar{\nu}$ decays [84], where currently only upper limits have been reported. Future measurements of these branching fractions are expected to achieve a precision of the order of 10% with 50 ab^{-1} of data [84]. The $\Lambda_b^0 \to \Lambda\nu\bar{\nu}$ decay process, on the other hand, requires high-energy experiments such as FCC-ee, often referred to as Tera-Z experiments. A more effective strategy, as discussed in Ref. [85], leverages the substantial missing energy imbalance between the signal and nonsignal hemispheres. The details of this approach can be found in Ref. [85]. To distinguish between signal-like and backgroundlike events, a two-stage boosted decision tree (BDT) approach has been implemented. The first BDT considers global event features, while the second focuses on candidate-specific information. By employing these BDTs, one can optimize selection criteria and assess the sensitivity to the $\Lambda_b \to \Lambda\nu\bar{\nu}$ signal. Recent analysis in Ref. [83] have shown that the reconstruction efficiency for Λ particles is approximately 80%. This enables the extrapolation of sensitivity estimates for the neutral modes, leading to expected sensitivities that are consistent with the SM predictions. These sensitivities can also be expressed as signal-to-background ratios. In Ref. [86], the authors have demonstrated that for the $\Lambda_b \to \Lambda\nu\bar{\nu}$ decay channel, the expected sensitivity stands at 9.86% with a signal-to-background ratio of 0.015. In summary, these comprehensive studies underscore the

TABLE III. $\Lambda_b \to \Lambda$ form factor inputs [49].

Parameter	Value	Parameter	Value
$a_0^{f_+}$	0.4221 ± 0.0188	$a_1^{g_0}$	-1.0290 ± 0.1614
$a_1^{f_+}$	-1.1386 ± 0.1683	$a_1^{g_\perp}$	-1.1357 ± 0.1911
$a_0^{f_0}$	0.3725 ± 0.0213	$a_0^{h_+}$	0.4960 ± 0.0258
$a_1^{f_0}$	-0.9389 ± 0.2250	$a_1^{h_+}$	-1.1275 ± 0.2537
$a_0^{f_\perp}$	0.5182 ± 0.0251	$a_0^{h_\perp}$	0.3876 ± 0.0172
$a_1^{f_\perp}$	-1.3495 ± 0.2413	$a_1^{h_\perp}$	-0.9623 ± 0.1550
$a_0^{g_\perp, g_+}$	0.3563 ± 0.0142	$a_0^{\tilde{h}_\perp, \tilde{h}_+}$	0.3403 ± 0.0133
$a_1^{g_+}$	-1.0612 ± 0.1678	$a_1^{\tilde{h}_+}$	-0.7697 ± 0.1612
$a_0^{g_0}$	0.4028 ± 0.0182	$a_1^{\tilde{h}_\perp}$	-0.8008 ± 0.1537
$m_{\rm pole}^{f_+}$, $m_{\rm pole}^{f_\perp}$, $m_{\rm pole}^{h_+}$, $m_{\rm pole}^{h_\perp}$	5.416	$m_{\rm pole}^{f_0}$	5.711
$m_{\rm pole}^{g_+}$, $m_{\rm pole}^{g_\perp}$, $m_{\rm pole}^{\tilde{h}_+}$, $m_{\rm pole}^{\tilde{h}_\perp}$	5.750	m_{g_0}	5.367

TABLE IV. SM predictions of branching ratio (BR), longitudinal polarization fraction F_L, lepton forward-backward asymmetry $A_{\rm FB}$, angular coefficients $\hat{K}_i'$s and ratio of branching ratio $R_{\Lambda^{(*)}}$ for the $\Lambda_b \to \Lambda^*(\to pK^-)\mu^+\mu^-$ and $\Lambda_b \to \Lambda(\to p\pi)\mu^+\mu^-$ decay channels.

		$\Lambda_b \to \Lambda^*(\to pK^-)\mu^+\mu^-$ decay		$\Lambda_b \to \Lambda(\to p\pi)\mu^+\mu^-$ decay	
Observables	q^2 bin	Central value	1σ range	Central value	1σ range
BR	1.1–6.0	6.063×10^{-9}	$(4.660, 8.012) \times 10^{-9}$	0.775×10^{-7}	$(0.460, 1.164) \times 10^{-7}$
	$14.2/15.0$-$q^2_{\rm max}$	7.318×10^{-9}	$(5.655, 9.100) \times 10^{-9}$	3.723×10^{-7}	$(3.105, 4.313) \times 10^{-7}$
F_L	1.1–6.0	0.781	(0.760, 0.800)	0.829	(0.696, 0.907)
	$14.2/15.0$-$q^2_{\rm max}$	0.430	(0.424, 0.443)	0.339	(0.312, 0.375)
$A_{\rm FB}$	1.1–6.0	−0.114	(−0.135, −0.089)	−0.028	(−0.146, 0.051)
	$14.2/15.0$-$q^2_{\rm max}$	−0.236	(−0.274, −0.198)	−0.299	(−0.330, −0.269)
$\hat{K}_{1c}$	1.1–6.0	−0.152	(−0.180, −0.119)	−0.019	(−0.097, 0.034)
	$14.2/15.0$-$q^2_{\rm max}$	−0.313	(−0.363, −0.262)	−0.199	(−0.220, −0.180)
$\hat{K}_{1cc}$	1.1–6.0	0.219	(0.200, 0.239)	0.086	(0.046, 0.152)
	$14.2/15.0$-$q^2_{\rm max}$	0.565	(0.552, 0.573)	0.331	(0.313, 0.344)
$\hat{K}_{1ss}$	1.1–6.0	0.890	(0.880, 0.900)	0.457	(0.424, 0.477)
	$14.2/15.0$-$q^2_{\rm max}$	0.713	(0.719, 0.710)	0.335	(0.328, 0.344)
$\hat{K}_{2c}$	1.1–6.0	−0.038	(−0.045, −0.030)	0.013	(−0.012, 0.063)
	$14.2/15.0$-$q^2_{\rm max}$	−0.080	(−0.093, −0.067)	0.202	(0.190, 0.210)
$\hat{K}_{2cc}$	1.1–6.0	0.055	(0.050, 0.060)	−0.054	(−0.095, −0.029)
	$14.2/15.0$-$q^2_{\rm max}$	0.145	(0.142, 0.146)	−0.135	(−0.149, −0.122)
$\hat{K}_{2ss}$	1.1–6.0	0.223	(0.220, 0.225)	−0.026	(−0.048, −0.012)
	$14.2/15.0$-$q^2_{\rm max}$	0.181	(0.180, 0.182)	−0.067	(−0.074, −0.061)
$\hat{K}_{4ss}$	1.1–6.0	0.000	(−0.001, 0.001)	×	×
	$14.2/15.0$-$q^2_{\rm max}$	−0.032	(−0.039, −0.027)	×	×
$\hat{K}_{4sc}$	1.1–6.0	×	×	0.003	(−0.062, 0.078)
	$14.2/15.0$-$q^2_{\rm max}$	×	×	−0.043	(−0.057, −0.030)
$\hat{K}_{4s}$	1.1–6.0	×	×	0.031	(−0.057, 0.110)
	$14.2/15.0$-$q^2_{\rm max}$	×	×	−0.116	(−0.132, −0.100)
$\hat{K}_{5s}$	1.1–6.0	0.014	(0.011, 0.018)	×	×
	$14.2/15.0$-$q^2_{\rm max}$	0.046	(0.039, 0.055)	×	×
$R_{\Lambda^{(*)}}$	1.1–6.0	0.996	(0.996, 0.996)	0.995	(0.989, 1.007)
	$14.2/15.0$-$q^2_{\rm max}$	0.993	(0.993,0.993)	1.007	(1.006, 1.007)
$\mathcal{Q}_{F_L}$	1.1–6.0	−0.000	(−0.000, −0.000)	−0.011	(−0.017, −0.007)
	$14.2/15.0$-$q^2_{\rm max}$	−0.000	(0.000, 0.000)	0.001	(0.001,0.001)
$\mathcal{Q}_{A_{\rm FB}}$	1.1–6.0	0.000	(0.000, 0.000)	0.001	(−0.000, 0.003)
	$14.2/15.0$-$q^2_{\rm max}$	0.001	(0.001, 0.001)	−0.000	(−0.000, −0.000)

TABLE V. SM prediction of $\Lambda_b \to \Lambda^*(\to pK^-)\nu\bar{\nu}$ and $\Lambda_b \to \Lambda(\to p\pi)\nu\bar{\nu}$ decay observables.

	$\Lambda_b \to \Lambda^*(\to pK^-)\nu\bar{\nu}$ decay		$\Lambda_b \to \Lambda(\to p\pi)\nu\bar{\nu}$ decay	
Observables	Central value	1σ range	Central value	1σ range
$\mathrm{BR}\times 10^{-6}$	1.414	(1.148, 1.743)	1.795	(1.406, 2.202)
F_L	0.522	(0.503, 0.547)	0.472	(0.395, 0.564)
$\hat{K}_{1c}$	−0.421	(−0.440, −0.391)	−0.207	(−0.165, −0.241)
$\hat{K}_{1cc}$	0.477	(0.452, 0.497)	0.264	(0.218, 0.302)
$\hat{K}_{1ss}$	0.760	(0.751, 0.773)	0.368	(0.349, 0.391)
$\hat{K}_{2c}$	−0.106	(−0.110, −0.098)	0.170	(0.140, 0.194)
$\hat{K}_{2cc}$	0.120	(0.114, 0.125)	−0.133	(−0.155, −0.106)
$\hat{K}_{2ss}$	0.190	(0.188, 0.193)	−0.066	(−0.077, −0.053)
$\hat{K}_{4sc}$	×	×	−0.032	(−0.060, 0.000)
$\hat{K}_{4s}$	×	×	−0.061	(−0.099, −0.025)
$\hat{K}_{4ss}$	−0.008	(−0.011, −0.006)	×	×
$\hat{K}_{5s}$	0.022	(0.019, 0.026)	×	×

exceptional and perhaps unparalleled opportunity offered by FCC-ee to measure these exceedingly rare and experimentally challenging, yet theoretically clean observables with exceptional precision.

C. χ^2 fit

Our primary objective in this work is to use a model-independent SMEFT formalism to investigate the effects of $b \to s\ell^+\ell^-$ anomalies on several baryonic $b \to s\ell^+\ell^-$ and $b \to s\nu\bar{\nu}$ transition decays. The SMEFT coefficients for left chiral currents, namely $\tilde{c}_{ql}^{(1)}$, $\tilde{c}_{ql}^{(3)}$, and $\tilde{c}_Z$ contribute to WCs $C_{9,10}$ in $b \to s\ell^+\ell^-$ and to C_L in $b \to s\nu\bar{\nu}$ transitions decays. Similarly, the SMEFT coefficients for right chiral currents such as $\tilde{c}_{dl}$ and $\tilde{c}'_Z$ are connected to $C'_{9,10}$ in $b \to s\ell^+\ell^-$ and C_R in $b \to s\nu\bar{\nu}$ transition decays. We construct several $1D$ and $2D$ NP scenarios. For $1D$ NP scenario, we consider NP contribution from a single NP operator, whereas, for $2D$ NP scenario, we consider NP contribution from two different NP operators simultaneously. We use a naive χ^2 analysis and determine the scenario that best explains the anomalies observed in $b \to s\ell^+\ell^-$ transition decays. We define our χ^2 as follows

$$\chi^2 = \sum_i \frac{(\mathcal{O}_i^{\rm th} - \mathcal{O}_i^{\rm exp})^2}{(\Delta\mathcal{O}_i^{\rm exp})^2 + (\Delta\mathcal{O}_i^{\rm th})^2}, \qquad (23)$$

where $\mathcal{O}_i^{\rm th}$ and $\mathcal{O}_i^{\rm exp}$ denote the theoretical and measured central values of each observables, respectively. The uncertainties associated with theory and experimental values are represented by $\Delta\mathcal{O}_i^{\rm th}$ and $\Delta\mathcal{O}_i^{\rm exp}$. In our χ^2 analysis, we include total eight measurements, namely $R_{K[q^2=1.1\text{–}6]}$, $R_{K^*[q^2=1.1\text{–}6]}$, $P'_{5[q^2=4\text{–}6]}$, $P'_{5[q^2=4.3\text{–}6]}$, $P'_{5[q^2=4\text{–}8]}$, $\mathcal{B}(B_s \to \phi\mu^+\mu^-)$, and $\mathcal{B}(B_s \to \mu^+\mu^-)$. The measured values of each observables considered for our analysis are reported in Table VI.

The best fit values and the corresponding allowed ranges of all the SMEFT coefficients for various $1D$ and $2D$ scenarios are reported in Table VII. We also report the

TABLE VI. Current experimental status of $b \to s\ell^+\ell^-$ and $b \to s\nu\bar{\nu}$ decay observables.

Observables	q^2 bins	Experimental measurements
R_K	[1.1, 6.0]	$0.846^{+0.044}_{-0.041}$ [1,87]
R_{K^*}	[1.1, 6.0]	$0.685^{+0.113}_{-0.069}(\mathrm{stat}) \pm 0.047(\mathrm{syst})$ [2]
		$0.96^{+0.45}_{-0.29}(\mathrm{stat}) \pm 0.11(\mathrm{syst})$ [4]
	[4.0, 6.0]	-0.21 ± 0.15 [9–11]
P'_5	[4.3, 6.0]	$-0.96^{+0.22}_{-0.21}(\mathrm{stat}) \pm 0.16(\mathrm{syst})$ [88]
	[4.0, 8.0]	$-0.267^{+0.275}_{-0.269}(\mathrm{stat}) \pm 0.049(\mathrm{syst})$ [13]
$dB/dq^2(B_s \to \phi\mu^+\mu^-)$	⋯	$(2.88 \pm 0.22) \times 10^{-8}$ [17–19] GeV^{-2}
$\mathcal{B}(B_s \to \mu^+\mu^-)$	⋯	$(3.09^{+0.46+0.15}_{-0.43-0.11}) \times 10^{-9}$ [89]
$\mathcal{B}(B^0 \to K^0\nu\nu)$	⋯	$<(1.1 \pm 0.4) \times 10^{-5}$ [21]
$\mathcal{B}(B^0 \to K^{0*}\nu\nu)$	⋯	$<2.7 \times 10^{-5}$ [90]

TABLE VII. Best fit values and the allowed ranges of SMEFT coefficients at 95% C.L. in several 1D and 2D scenarios.

SMEFT couplings	Best fit	$\chi^2_{\rm min}$/d.o.f	Pull$_{\rm SM}$
SM	...	5.578	...
$\tilde{c}_{ql}^{(1),(3)}$	−0.495	2.953	1.620
$1\sigma \rightarrow$	[−8.683, 0.335]		
$\tilde{c}_Z$	0.862	3.374	1.484
$1\sigma \rightarrow$	[−0.529, 9.599]		
$\tilde{c}'_Z$	−0.114	6.728	...
$1\sigma \rightarrow$	[−1.106, 1.027]		
$\tilde{c}_{dl}$	−0.114	6.954	...
$1\sigma \rightarrow$	[−0.696, 0.693]		
$(\tilde{c}_{ql}^{(1)}, \tilde{c}_{ql}^{(3)})$	(−9.444, 8.797)	3.391	1.478
$1\sigma \rightarrow$	([−9.999, 9.969], [−9.998, 9.937])		
$(\tilde{c}_{ql}^{(1),(3)}, \tilde{c}_Z)$	(−1.732, −1.608)	3.211	1.539
$1\sigma \rightarrow$	([−8.951, 2.619], [−5.293, 8.713])		
$(\tilde{c}_{ql}^{(1),(3)}, \tilde{c}_{dl})$	(−0.660, 0.211)	4.324	1.120
$1\sigma \rightarrow$	([−8.457, 0.175], [−2.333, 1.128])		
$(\tilde{c}_{ql}^{(1),(3)}, \tilde{c}'_Z)$	(−3.774, −4.827)	1.402	2.044
$1\sigma \rightarrow$	([−8.431, 0.175], [−6.038, 5.537])		
$(\tilde{c}_Z, \tilde{c}_{dl})$	(0.969, 0.211)	4.679	0.948
$1\sigma \rightarrow$	([−0.167, 4.647], [−0.749, 1.837])		
$(\tilde{c}_Z, \tilde{c}'_Z)$	(4.492, −4.057)	1.863	1.927
$1\sigma \rightarrow$	([−0.195, 6.346], [−5.175, 4.725])		
$(\tilde{c}_{dl}, \tilde{c}'_Z)$	(−0.105, −0.164)	8.395	...
$1\sigma \rightarrow$	([−2.616, 1.341], [−1.634, 0.881])		
$(\tilde{c}_{ql}^{(1)} + \tilde{c}_{ql}^{(3)}$	−0.495	2.953	1.620
$1\sigma \rightarrow$	[0.343, 1.157]		
$(\tilde{c}_{ql}^{(1)} + \tilde{c}_{ql}^{(3)}, \tilde{c}_Z)$	(−1.119, −0.804)	3.383	1.482
$1\sigma \rightarrow$	([−8.804, 2.655], [−5.422, 8.742])		
$(\tilde{c}_{ql}^{(1)} + \tilde{c}_{ql}^{(3)}, \tilde{c}_{dl})$	(−0.645, −0.010)	3.671	1.381
$1\sigma \rightarrow$	([−8.453, 0.157], [−2.323, 1.084])		
$(\tilde{c}_{ql}^{(1)} + \tilde{c}_{ql}^{(3)}, \tilde{c}'_Z)$	(−3.776, −4.938)	1.417	2.040
$1\sigma \rightarrow$	([−8.447, 0.157], [−6.078, 5.545])		

$\chi^2_{\rm min}$/d.o.f and the Pull$_{\rm SM} = \sqrt{\chi^2_{\rm SM} - \chi^2_{\rm NP}}$ for each scenario in Table VII. We consider eight measured parameters in our χ^2 analysis. Hence, the number of degrees of freedom (d.o.f) will be $8 - 1 = 7$ for each 1D NP scenario and $8 - 2 = 6$ for each 2D NP scenario. We first determine the $\chi^2_{\rm min}$/d.o.f in the SM to be 5.578, which determines the degree of disagreement between the SM prediction and the current experimental data. In each case, the $\chi^2_{\rm min}$ value represents the best-fit value. We impose $\chi^2 \leq 12.592$ constraint to obtain the allowed range of each 1D NP coefficient at 95% percent confidence level (C.L.). Similarly, the allowed range for each 2D NP coefficient at the 95% CL is obtained by imposing $\chi^2 \leq 11.070$ constraint.

It is evident from Table VII that not all the SMEFT coefficients can explain the observed deviations in $b \rightarrow s\ell^+\ell^-$ data. In fact, NP scenarios represented by $\tilde{c}_{dl}$, $\tilde{c}'_Z$ and $(\tilde{c}_{dl}, \tilde{c}'_Z)$ WC's are ruled out because the $\chi^2_{\rm min}$ values obtained for these scenarios are higher than the χ^2 value obtained in SM. Hence, we will not discuss them any further. Nevertheless, there are a few 2D scenarios, namely $(\tilde{c}_{ql}^{(3)}, \tilde{c}'_Z)$, $(\tilde{c}_Z, \tilde{c}'_Z)$, and $(\tilde{c}_{ql}^{(1)} + \tilde{c}_{ql}^{(3)}, \tilde{c}'_Z)$, for which the Pull$_{\rm SM}$ is considerably larger than the rest of the NP scenarios. Furthermore, these scenarios exhibit better compatibility with R_K, R_{K^*}, P'_5, $\mathcal{B}(B_s \rightarrow \phi\mu^+\mu^-)$ and $\mathcal{B}(B_s \rightarrow \mu^+\mu^-)$ data. In Table VIII, we present the central values and the corresponding 1σ uncertainties associated with each observable pertaining to $B \rightarrow, K^{(*)}\mu^+\mu^-$ decays in the SM and in case of several NP scenarios. The experimental values till 2022 December for R_K, $R_{K^*[q^2=1.1\text{–}6]}$, $P'_{5[q^2=4\text{–}6]}$, $P'_{5[q^2=4.3\text{–}6]}$, $P'_{5[q^2=4\text{–}8]}$, $\mathcal{B}(B_s \rightarrow \phi\mu^+\mu^-)$, and $\mathcal{B}(B_s \rightarrow \mu^+\mu^-)$ are also listed in the first row of Table VIII.

TABLE VIII. Best fit values and the corresponding allowed ranges of R_K, R_{K^*}, P_5' [4.0, 6.0], P_5' [4.3, 6.0], P_5' [4.0, 8.0], $\mathcal{B}(B_s \to \phi\mu^+\mu^-)$ and $\mathcal{B}(B_s \to \mu^+\mu^-)$ with each NP scenarios of Table VII.

SMEFT couplings	R_K	R_{K^*}	P_5' [4.0,6.0]	P_5' [4.3, 6.0]	P_5' [4.0, 8.0]	$\mathcal{B}(B_s \to \phi\mu\mu) \times 10^{-7}$	$\mathcal{B}(B_s \to \mu\mu) \times 10^{-9}$
$\tilde{c}_{ql}^{(3)}$	0.792	0.791	−0.693	−0.702	−0.719	2.314	3.108
1σ	(0.343, 1.157)	(0.359, 1.352)	(−0.985, −0.500)	(−0.986, −0.524)	(−0.991, −0.591)	(1.089, 4.127)	(1.179, 4.549)
$\tilde{c}_Z$	0.810	0.784	−0.768	−0.775	−0.778	2.227	2.548
1σ	(0.429, 1.146)	(0.348, 1.151)	(−1.062, 0.761)	(−1.064, 0.770)	(−1.040, 0.793)	(1.065, 4.094)	(0.146, 4.869)
$(\tilde{c}_{ql}^{(1)}, \tilde{c}_{ql}^{(3)})$	0.737	0.731	−0.672	−0.682	−0.705	2.190	2.883
1σ	(0.412, 1.094)	(0.421, 1.185)	(−0.975, −0.535)	(−0.976, −0.552)	(−0.980, −0.603)	(1.269, 3.827)	(1.575, 4.290)
$(\tilde{c}_{ql}^{(1),(3)}, \tilde{c}_Z)$	0.694	0.751	−0.491	−0.508	−0.569	2.160	3.622
1σ	(0.363, 1.102)	(0.427, 1.218)	(−1.041, 0.530)	(−1.042, 0.544)	(−1.020, 0.598)	(1.275, 3.721)	(0.000, 6.022)
$(\tilde{c}_{ql}^{(1),(3)}, \tilde{c}_Z')$	0.825	0.594	−0.329	−0.314	−0.255	1.756	2.838
1σ	(0.353, 1.330)	(0.223, 1.151)	(−1.170, 0.518)	(−1.178, 0.507)	(−1.179, 0.464)	(0.643, 3.799)	(0.000, 5.717)
$(\tilde{c}_Z, \tilde{c}_Z')$	0.900	0.709	−0.311	−0.295	−0.227	2.073	2.717
1σ	(0.379, 1.300)	(0.351, 1.131)	(−1.187, 0.592)	(−1.186, 0.576)	(−1.149, 0.502)	(1.054, 3.910)	(0.023,5.466)
$(\tilde{c}_{ql}^{(1)} + \tilde{c}_{ql}^{(3)}, \tilde{c}_Z)$	0.733	0.754	−0.589	−0.601	−0.637	2.327	3.494
1σ	(0.363, 1.109)	(0.422, 1.161)	(−1.012, 0.532)	(−1.013, 0.546)	(−1.000, 0.605)	(1.255, 3.730)	(0.000, 5.993)
$(\tilde{c}_{ql}^{(1)} + \tilde{c}_{ql}^{(3)}, \tilde{c}_{dl})$	0.734	0.737	−0.661	−0.672	−0.701	2.322	2.851
1σ	(0.387, 1.205)	(0.271, 1.135)	(−1.141, −0.161)	(−1.146, −0.161)	(−1.146, −0.159)	(−1.166, −0.013)	(0.804, 3.679)
$(\tilde{c}_{ql}^{(1)} + \tilde{c}_{ql}^{(3)}, \tilde{c}_Z')$	0.855	0.611	−0.280	−0.266	−0.211	1.785	3.006
1σ	(0.360, 1.317)	(0.215, 1.163)	(−1.173, 0.522)	(−1.179, 0.511)	(−1.179, 0.468)	(0.664, 3.757)	(0.000, 5.868)

We now move to analyse the goodness of our fit results with the measured values of $\mathcal{B}(B \to K^{(*)}\nu\bar{\nu})$. We report, in Table IX, the best fit values and the corresponding allowed ranges of $\mathcal{B}(B \to K^{(*)}\nu\bar{\nu})$, $F_L^{K^*}$ and also the ratios $\mathcal{R}_{\mathcal{K}}$, $\mathcal{R}_{\mathcal{K}^*}$ and $\mathcal{R}_{\mathcal{F}_\mathcal{L}}^{\mathcal{K}^*}$ obtained with the best fit values and the allowed ranges of each NP couplings at 95% C.L. of Table VII. We also report the SM central values and the corresponding 1σ uncertainties associated with each observable in Table IX. In the SM, the branching fractions of $B \to K^{(*)}\nu\bar{\nu}$ decays are of $\mathcal{O}(10^{-6})$. The ratios $\mathcal{R}_{\mathcal{K}}$, $\mathcal{R}_{\mathcal{K}^*}$ and $\mathcal{R}_{\mathcal{F}_\mathcal{L}}^{\mathcal{K}^*}$ are equal to unity in the SM. Hence any deviation from unity in these parameters could be a clear signal of beyond the SM physics. Moreover, there exists a few experiments that provide the upper bound on the branching ratio of $B \to K^{(*)}\nu\bar{\nu}$ to be $\mathcal{B}(B \to K\nu\bar{\nu}) < 11 \times 10^{-6}$ and $\mathcal{B}(B \to K^*\nu\bar{\nu}) < 27 \times 10^{-6}$, respectively. Ignoring any theoretical uncertainty, we estimate the upper bound on $\mathcal{R}_{\mathcal{K}}^{(*)}$ to be $\mathcal{R}_{\mathcal{K}} < 2.75$ and $\mathcal{R}_{\mathcal{K}^*} < 2.89$, respectively.

We observe that the range of $B \to K^{(*)}\nu\bar{\nu}$ and $\mathcal{R}_{\mathcal{K}}^{(*)}$ obtained with the allowed range of each NP couplings are compatible with the experimental upper bound of $B \to K^{(*)}\nu\bar{\nu}$ and $\mathcal{R}_{\mathcal{K}}^{(*)}$. However, the best fit values of $B \to K^{(*)}\nu\bar{\nu}$ and $\mathcal{R}_{\mathcal{K}}^{(*)}$ obtained with the best fit values of $(\tilde{c}_{ql}^{(1)}, \tilde{c}_{ql}^{(3)})$, $(\tilde{c}_{ql}^{(1)}, \tilde{c}_Z')$, and $(\tilde{c}_{ql}^{(1)} + \tilde{c}_{ql}^{(3)}, \tilde{c}_Z')$ SMEFT coefficients are larger than the experimental upper bound. Hence a simultaneous explanation of $b \to s\ell^+\ell^-$ and $b \to s\nu\bar{\nu}$ is not possible with these NP scenarios. Moreover, the values of $B \to K^{(*)}\nu\bar{\nu}$ and $\mathcal{R}_{\mathcal{K}}^{(*)}$ obtained with $(\tilde{c}_{ql}^{(1)}, \tilde{c}_Z)$ SMEFT coefficients are quite large. More precise measurement on $B \to K^{(*)}\nu\bar{\nu}$ branching fraction in future can exclude this NP scenario.

Again it can be seen from Table IX that $\mathcal{R}_{\mathcal{F}_\mathcal{L}}^{\mathcal{K}^*}$ remains SM like for all the scenarios with left handed currents. However, with the inclusion of right handed currents, its value seem to differ from unity. Hence a deviation from unity in $\mathcal{R}_{\mathcal{F}_\mathcal{L}}^{\mathcal{K}^*}$ would be clear signal of NP through right handed currents. It should be emphasized that the value of $\mathcal{R}_{\mathcal{F}_\mathcal{L}}^{\mathcal{K}^*}$ obtained with $(\tilde{c}_{ql}^{(1)}, \tilde{c}_Z')$, $(\tilde{c}_{ql}^{(3)}, \tilde{c}_Z')$, $(\tilde{c}_Z, \tilde{c}_Z')$, and $(\tilde{c}_{ql}^{(1)} + \tilde{c}_{ql}^{(3)}, \tilde{c}_Z')$ SMEFT couplings deviates significantly from the SM prediction.

In Fig. 1, we show the allowed ranges of $\mathcal{B}(B \to K^{(*)}\nu\bar{\nu})$ with few selected NP scenarios such as $(\tilde{c}_{ql}^{(1)}, \tilde{c}_Z')$, $(\tilde{c}_{ql}^{(3)}, \tilde{c}_Z')$, $(\tilde{c}_Z, \tilde{c}_Z')$, and $(\tilde{c}_{ql}^{(1)} + \tilde{c}_{ql}^{(3)}, \tilde{c}_Z')$ that best explains the $b \to s\ell^+\ell^-$ data. Best fit values of $\mathcal{B}(B \to K^{(*)}\nu\bar{\nu})$ are shown with a black dot in Fig. 1. The allowed range of each observable is obtained by using the allowed ranges of the NP couplings. The red and green line represents the experimental upper bound of $\mathcal{B}(B \to K\nu\bar{\nu})$ and $\mathcal{B}(B \to K^*\nu\bar{\nu})$, respectively. It is evident that the allowed ranges of $\mathcal{B}(B \to K\nu\bar{\nu})$ and $\mathcal{B}(B \to K^*\nu\bar{\nu})$ obtained with $(\tilde{c}_{ql}^{(3)}, \tilde{c}_Z')$ and $(\tilde{c}_Z, \tilde{c}_Z')$ SMEFT scenarios are compatible with the experimental upper bound. In case of $(\tilde{c}_{ql}^{(1)}, \tilde{c}_Z')$ and $(\tilde{c}_{ql}^{(1)} + \tilde{c}_{ql}^{(3)}, \tilde{c}_Z')$ NP scenarios, although the best fit value does not simultaneously satisfy the experimental upper bound, there still exist some NP parameter space that can, in principle, satisfy both the constraint. It is also evident that, the best fit value of $\mathcal{B}(B \to K\nu\bar{\nu}) = 12.9 \times 10^{-6}$

TABLE IX. Best fit values and the corresponding allowed ranges of $\mathcal{B}(B \to K^{(*)}\nu\bar{\nu})$, $F_L^{K^*}$ and the ratios $\mathcal{R}_{\mathcal{K}}$, $\mathcal{R}_{\mathcal{K}^*}$, and $\mathcal{R}_{\mathcal{F}_{\mathcal{L}}}^{\mathcal{K}^*}$ in SM and in the presence of NP scenarios of Table VII.

SMEFT couplings	$\mathcal{B}(B \to K\nu\bar{\nu}) \times 10^{-6}$	$\mathcal{R}_{\mathcal{K}}$	$\mathcal{B}(B \to K^*\nu\bar{\nu}) \times 10^{-6}$	$\mathcal{R}_{\mathcal{K}^*}$	$F_L(B \to K^*\nu\bar{\nu})$	$\mathcal{R}_{\mathcal{F}_{\mathcal{L}}}^{\mathcal{K}^*}$
SM	4.006 ± 0.261	1.000	9.331 ± 0.744	1.000	0.493 ± 0.038	1.000
$\tilde{c}_{ql}^{(1)}$	4.490	1.162	10.690	1.162	0.427	1.000
$1\sigma \to$	(3.105, 25.688)	(0.897, 5.602)	(6.974, 62.949)	(0.897, 5.602)	(0.372, 0.617)	(1.000, 1.000)
$\tilde{c}_{ql}^{(3)}$	3.285	0.850	7.821	0.850	0.427	1.000
$1\sigma \to$	(0.071, 5.079)	(0.020, 1.108)	(0.181, 12.116)	(0.020, 1.108)	(0.372, 0.617)	(1.000, 1.000)
$\tilde{c}_Z$	3.283	0.747	7.095	0.747	0.465	1.000
$1\sigma \to$	(0.364, 5.135)	(0.090, 1.174)	(0.796, 12.854)	(0.090, 1.174)	(0.374, 0.631)	(1.000, 1.000)
$(\tilde{c}_{ql}^{(1)}, \tilde{c}_{ql}^{(3)})$	61.985	14.989	160.627	14.989	0.488	1.000
$1\sigma \to$	(0.000, 76.129)	(0.000, 17.069)	(0.000, 179.628)	(0.000, 17.069)	(0.366, 0.614)	(1.000, 1.000)
$(\tilde{c}_{ql}^{(1)}, \tilde{c}_Z)$	9.349	2.328	19.468	2.328	0.458	1.000
$1\sigma \to$	(0.000, 28.557)	(0.000, 7.123)	(0.000, 72.582)	(0.000, 7.123)	(0.368, 0.617)	(1.000, 1.000)
$(\tilde{c}_{ql}^{(3)}, \tilde{c}_Z)$	3.860	0.961	8.038	0.961	0.458	1.000
$1\sigma \to$	(0.053, 6.019)	(0.015, 1.387)	(0.143, 14.583)	(0.015, 1.387)	(0.368, 0.617)	(1.000, 1.000)
$(\tilde{c}_{ql}^{(1)}, \tilde{c}_{dl})$	4.784	1.146	12.868	1.271	0.471	1.017
$1\sigma \to$	(2.991, 26.517)	(0.868, 6.037)	(7.790, 58.665)	(0.940, 5.291)	(0.348, 0.622)	(0.822, 1.088)
$(\tilde{c}_{ql}^{(3)}, \tilde{c}_{dl})$	3.108	0.745	8.565	0.846	0.472	1.021
$1\sigma \to$	(0.000, 4.735)	(0.000, 1.088)	(0.373, 10.768)	(0.045, 1.084)	(0.362, 0.685)	(0.893, 1.248)
$(\tilde{c}_{ql}^{(1)}, \tilde{c}'_Z)$	22.421	5.541	12.148	1.527	0.236	0.456
$1\sigma \to$	(2.991, 30.806)	(0.812, 6.835)	(7.484, 79.139)	(0.863, 6.891)	(0.113, 0.685)	(0.262, 1.224)
$(\tilde{c}_{ql}^{(3)}, \tilde{c}'_Z)$	5.499	1.359	2.681	0.337	0.193	0.372
$1\sigma \to$	(0.140, 8.659)	(0.037, 1.951)	(0.140, 10.852)	(0.016, 1.150)	(0.000, 0.665)	(0.000, 1.170)
$(\tilde{c}_Z, \tilde{c}_{dl})$	2.361	0.663	6.629	0.759	0.469	1.022
$1\sigma \to$	(0.001, 4.700)	(0.000, 1.149)	(1.481, 11.080)	(0.179, 1.076)	(0.364, 0.705)	(0.862, 1.266)
$(\tilde{c}_Z, \tilde{c}'_Z)$	3.191	0.868	2.312	0.238	0.258	0.502
$1\sigma \to$	(0.000, 6.147)	(0.000, 1.375)	(0.398, 11.688)	(0.042, 1.128)	(0.000, 0.706)	(0.000, 1.269)
$(\tilde{c}_{ql}^{(1)} + \tilde{c}_{ql}^{(3)}, \tilde{c}_Z)$	5.234	1.269	12.505	1.269	0.431	1.000
$1\sigma \to$	(0.000, 14.409)	(0.000, 3.436)	(0.000, 39.087)	(0.000, 3.436)	(0.371, 0.612)	(1.000, 1.000)
$(\tilde{c}_{ql}^{(1)} + \tilde{c}_{ql}^{(3)}, \tilde{c}_{dl})$	4.091	1.003	9.883	0.998	0.509	0.999
$1\sigma \to$	(2.415, 8.104)	(0.688, 1.865)	(5.307, 13.180)	(0.633, 1.283)	(0.294, 0.635)	(0.617, 1.100)
$(\tilde{c}_{ql}^{(1)} + \tilde{c}_{ql}^{(3)}, \tilde{c}'_Z)$	12.906	3.159	5.752	0.586	0.042	0.085
1σ	(0.060, 17.140)	(0.016, 3.829)	(4.165, 31.904)	(0.416, 3.068)	(0.001, 0.708)	(0.003, 1.285)

obtained with $(\tilde{c}_{ql}^{(1)} + \tilde{c}_{ql}^{(3)}, \tilde{c}'_Z)$ NP coupling is very close to the experimental upper bound of 11×10^{-6}.

D. Effects of SMEFT coefficients in $\Lambda_b \to \Lambda^*(\to pK^-)\mu^+\mu^-$ and $\Lambda_b \to \Lambda(\to p\pi)\mu^+\mu^-$ decay observables

Our main objective is to investigate NP effects on $\Lambda_b \to \Lambda^*(\to pK^-)\mu^+\mu^-$ and $\Lambda_b \to \Lambda(\to p\pi)\mu^+\mu^-$ decay observables in a model independent SMEFT framework. Based on our χ^2 analysis and the constraint imposed by the experimental upper bound of $\mathcal{B}(B \to K\nu\bar{\nu})$ and $\mathcal{B}(B \to K^*\nu\bar{\nu})$, we chose three NP scenarios namely, $(\tilde{c}_{ql}^{(3)}, \tilde{c}'_Z)$, $(\tilde{c}_Z, \tilde{c}'_Z)$, and $(\tilde{c}_{ql}^{(1)} + \tilde{c}_{ql}^{(3)}, \tilde{c}'_Z)$ that corresponds to larger $\mathrm{Pull}_{\mathrm{SM}}$ value than the rest of the NP scenarios. The results are listed in Tables X–XIII, respectively. Our observations are as follows

(i) *BR*: In case of $\Lambda_b \to \Lambda^*(\to pK^-)\mu^+\mu^-$ decay, branching ratio deviates from the SM prediction by almost 2σ deviation is observed in the presence of $(\tilde{c}_{ql}^{(1)} + \tilde{c}_{ql}^{(3)}, \tilde{c}'_Z)$ coupling at the high q^2 region. In case of $\Lambda_b \to \Lambda(\to p\pi)\mu^+\mu^-$ decay channel, no significant deviation is observed at low q^2 region. However, at high q^2 region, there is more than 1σ deviation in presence of $(\tilde{c}_Z, \tilde{c}'_Z)$ and $(\tilde{c}_{ql}^{(1)} + \tilde{c}_{ql}^{(3)}, \tilde{c}'_Z)$ NP couplings. Moreover, with $(\tilde{c}_{ql}^{(3)}, \tilde{c}'_Z)$ NP coupling, the deviation from the SM prediction is quite significant and it is distinguishable from the SM prediction at more than 5σ.

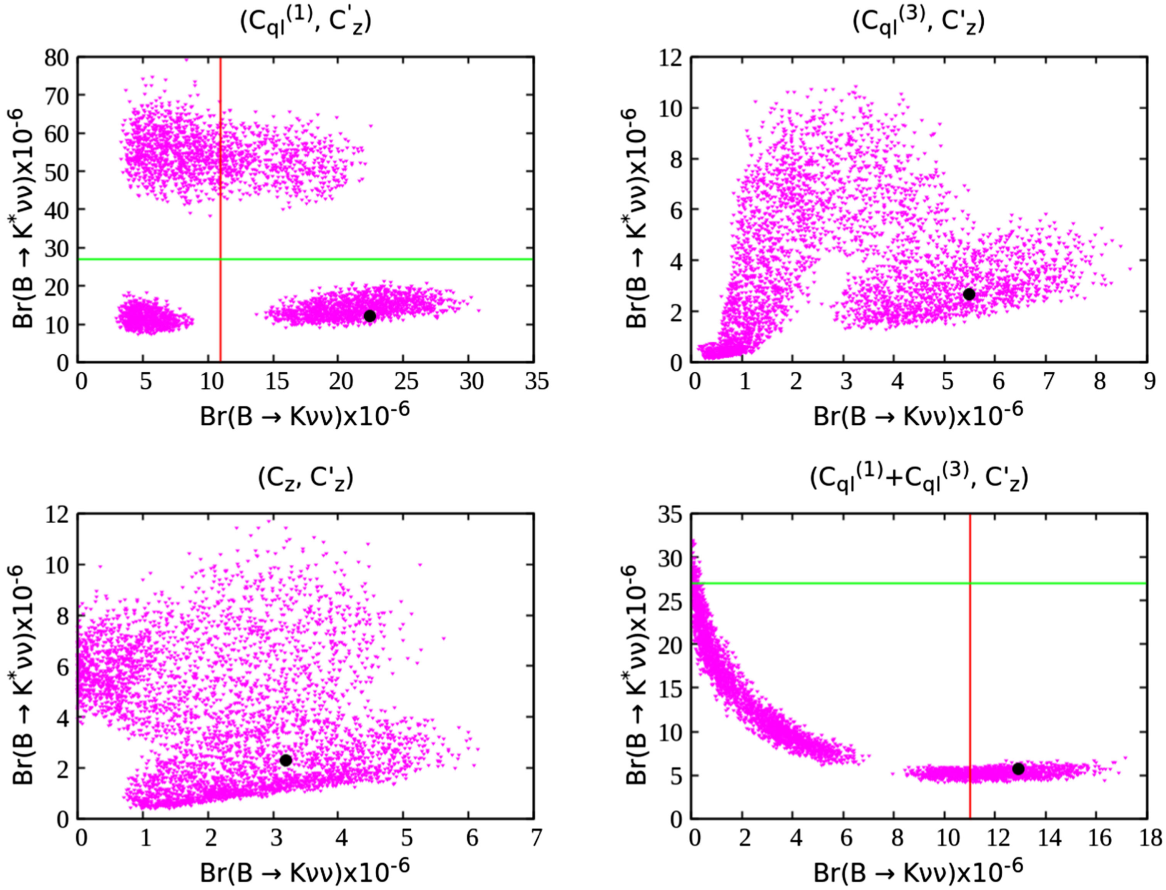

FIG. 1. Best fit values (black dot) and the corresponding allowed ranges of $\mathcal{B}(B \to K\nu\bar{\nu})$ and $\mathcal{B}(B \to K^*\nu\bar{\nu})$ in case of $(\tilde{c}_{ql}^{(1)}, \tilde{c}'_Z)$, $(\tilde{c}_{ql}^{(3)}, \tilde{c}'_Z)$, $(\tilde{c}_Z, \tilde{c}'_Z)$, and $(\tilde{c}_{ql}^{(1)} + \tilde{c}_{ql}^{(3)}, \tilde{c}'_Z)$ NP scenarios. The red and green line represents the experimental upper bound of $\mathcal{B}(B \to K\nu\bar{\nu}) < 11 \times 10^{-6}$ and $\mathcal{B}(B \to K^*\nu\bar{\nu}) < 27 \times 10^{-6}$, respectively.

(ii) F_L: For the $\Lambda_b \to \Lambda^*(\to pK^-)\mu^+\mu^-$ decay channel, F_L deviates from the SM prediction by 1σ in the presence of $(\tilde{c}_Z, \tilde{c}'_Z)$ NP couplings at the low q^2 region. Moreover, a significant deviation of more than 3σ is observed in the presence of $(\tilde{c}_{ql}^{(3)}, \tilde{c}'_Z)$ and $(\tilde{c}_{ql}^{(1)} + \tilde{c}_{ql}^{(3)}, \tilde{c}'_Z)$ NP couplings. At the high q^2 region, F_L deviates more than 2.8σ and 1.75σ in the presence of $(\tilde{c}_Z, \tilde{c}'_Z)$ and $(\tilde{c}_{ql}^{(1)} + \tilde{c}_{ql}^{(3)}, \tilde{c}'_Z)$ NP couplings, respectively. Similarly, a deviation of more than 3.5σ is observed in the presence of $(\tilde{c}_{ql}^{(3)}, \tilde{c}'_Z)$ NP coupling. In case of $\Lambda_b \to \Lambda^*(\to p\pi)\mu^+\mu^-$ channel, a deviation of more than 1σ is observed with $(\tilde{c}_{ql}^{(3)}, \tilde{c}'_Z)$ NP coupling at both low and high q^2 region.

(iii) A_{FB}: For the $\Lambda_b \to \Lambda^*(\to pK^-)\mu^+\mu^-$ decay, a significant deviation of more than 5σ from the SM prediction is observed in all the three NP scenarios at both low and high q^2 region. For the $\Lambda_b \to \Lambda(\to p\pi)\mu^+\mu^-$ decay channel, the deviation from the SM prediction is observed to be 1σ in the presence of $(\tilde{c}_{ql}^{(3)}, \tilde{c}'_Z)$ and $(\tilde{c}_{ql}^{(1)} + \tilde{c}_{ql}^{(3)}, \tilde{c}'_Z)$ coupling in the low q^2 region, whereas, at the high q^2 region, a deviation of more than 10σ is observed in case of all the NP scenarios.

(iv) $R_{\Lambda^{(*)}}$: We observe a deviation of more than 5σ and 10σ from the SM prediction in the ratio of branching fractions for the $\Lambda_b \to \Lambda^*(\to pK^-)\mu^+\mu^-$ and $\Lambda_b \to \Lambda(\to p\pi)\mu^+\mu^-$ decay channels in case all the NP scenarios at both low and high q^2 region.

(v) $\hat{K}_{1c}$: For the $\Lambda_b \to \Lambda^*(\to pK^-)\mu^+\mu^-$ decay channel, the angular observable $\hat{K}_{1c}$ deviates from the SM prediction at more than 5σ significance in the presence of $(\tilde{c}_{ql}^{(3)}, \tilde{c}'_Z)$, $(\tilde{c}_Z, \tilde{c}'_Z)$, and $(\tilde{c}_{ql}^{(1)} + \tilde{c}_{ql}^{(3)}, \tilde{c}'_Z)$ NP couplings at the low and high q^2 regions. For the $\Lambda_b \to \Lambda(\to p\pi)\mu^+\mu^-$ decay channel, 1σ deviation from the SM prediction is observed at low q^2 region with the $(\tilde{c}_Z, \tilde{c}'_Z)$ and $(\tilde{c}_{ql}^{(1)} + \tilde{c}_{ql}^{(3)}, \tilde{c}'_Z)$ NP couplings, whereas, at high q^2 region, a deviation of more than 10σ is observed

TABLE X. The branching ratio (BR), longitudinal polarization fraction F_L, lepton forward backward asymmetry A_{FB} and the ratio of branching ratio R_{Λ^*} for the $\Lambda_b \to \Lambda^*(\to pK^-)\mu^+\mu^-$ decay mode in case of few selected $2D$ NP scenarios.

$\Lambda_b \to \Lambda^*(\to pK^-)\mu^+\mu^-$ decay (μ mode)					
SMEFT couplings		BR $\times 10^{-9}$	F_L	A_{FB}	R_{Λ^*}
$(\tilde{c}_{ql}^{(3)}, \tilde{c}'_Z)$	1.1–6.0	4.785 [0.294, 14.542]	0.706 [0.051, 0.804]	0.056 [−0.276, 0.316]	0.786 [0.014, 2.100]
	$14.2 - q^2_{max}$	3.972 [0.263, 22.544]	0.477 [0.325, 0.558]	0.028 [−0.351, 0.091]	0.539 [0.008, 4.414]
$(\tilde{c}_Z, \tilde{c}'_Z)$	1.1–6.0	5.102 [1.453, 12.108]	0.802 [0.738, 0.910]	0.017 [−0.131, 0.087]	0.838 [0.085, 1.782]
	$14.2 - q^2_{max}$	4.921 [2.085, 19.113]	0.393 [0.344, 0.528]	0.001 [−0.352, 0.201]	0.668 [0.075, 3.464]
$(\tilde{c}_{ql}^{(1)} + \tilde{c}_{ql}^{(3)}, \tilde{c}'_Z)$	1.1–6.0	4.990 [0.293, 14.580]	0.707 [0.048, 0.804]	0.055 [−0.277, 0.314]	0.820 [0.013, 2.124]
	$14.2 - q^2_{max}$	4.165 [0.266, 22.458]	0.476 [0.559, 0.325]	0.029 [−0.351, 0.093]	0.565 [0.008,4.397]

TABLE XI. Angular observables $\hat{K}_i$ for the $\Lambda_b \to \Lambda^*(\to pK^-)\mu^+\mu^-$ decay mode in case of few selected $2D$ NP scenarios.

$\Lambda_b \to \Lambda^*(\to pK^-)\mu^+\mu^-$ decay (μ mode)									
SMEFT couplings	q^2 bin	$\hat{K}_{1c}$	$\hat{K}_{1cc}$	$\hat{K}_{1ss}$	$\hat{K}_{2c}$	$\hat{K}_{2cc}$	$\hat{K}_{2ss}$	$\hat{K}_{4ss}$	$\hat{K}_{5s}$
$(\tilde{c}_{ql}^{(3)}, \tilde{c}'_Z)$	1.1–6.0	0.074 [−0.369, 0.422]	0.294 [0.196, 0.949]	0.853 [0.525, 0.902]	0.019 [−0.092, 0.105]	0.074 [0.049, 0.237]	0.213 [0.131, 0.225]	−0.000 [−0.001, 0.001]	−0.007 [−0.010, 0.023]
	$14.2 - q^2_{max}$	0.518 [−0.465, 0.123]	0.736 [0.430, 0.672]	0.009 [0.661, 0.773]	0.134 [−0.119, 0.030]	0.182 [0.116, 0.170]	0.008 [0.160, 0.185]	−0.046 [−0.049, 0.036]	0.539 [−0.054, 0.067]
$(\tilde{c}_Z, \tilde{c}'_Z)$	1.1–6.0	0.023 [−0.174, 0.116]	0.198 [0.090, 0.262]	0.901 [0.869, 0.955]	0.006 [−0.044, 0.029]	0.050 [0.023, 0.066]	0.225 [0.215, 0.239]	0.000 [−0.001, 0.001]	−0.005 [−0.013, 0.017]
	$14.2 - q^2_{max}$	0.001 [−0.467, 0.266]	0.601 [0.459, 0.653]	0.694 [0.670, 0.758]	0.000 [−0.119, 0.068]	0.155 [0.124, 0.166]	0.175 [0.169, 0.188]	−0.002 [−0.047, 0.007]	−0.016 [−0.054, 0.065]
$(\tilde{c}_{ql}^{(1)} + \tilde{c}_{ql}^{(3)}, \tilde{c}'_Z)$	1.1–6.0	0.073 [−0.369, 0.419]	0.293 [0.196, 0.951]	0.854 [0.524, 0.902]	0.018 [−0.092, 0.105]	0.073 [0.049, 0.238]	0.213 [0.131, 0.225]	−0.000 [−0.001, 0.001]	−0.007 [−0.010, 0.023]
	$14.2 - q^2_{max}$	0.038 [−0.465, 0.126]	0.519 [0.429, 0.671]	0.735 [0.661, 0.773]	0.010 [−0.119, 0.030]	0.134 [0.116, 0.170]	0.182 [0.160, 0.185]	0.030 [−0.049, 0.036]	−0.046 [−0.049, 0.067]

with $(\tilde{c}_Z, \tilde{c}'_Z)$, $(\tilde{c}_{ql}^{(3)}, \tilde{c}'_Z)$, and $(\tilde{c}_{ql}^{(1)} + \tilde{c}_{ql}^{(3)}, \tilde{c}'_Z)$ NP couplings.

(vi) $\hat{K}_{1cc}$: In case of $\Lambda_b \to \Lambda^*(\to pK^-)\mu^+\mu^-$ decay channel, in the presence of $(\tilde{c}_{ql}^{(3)}, \tilde{c}'_Z)$ and $(\tilde{c}_{ql}^{(1)} + \tilde{c}_{ql}^{(3)}, \tilde{c}'_Z)$ NP couplings the angular observable $\hat{K}_{1cc}$ deviates from the SM prediction at more than 3σ at the low q^2 region, whereas, it deviates more than 10σ at the high q^2 region. For the $\Lambda_b \to \Lambda (\to p\pi)\mu^+\mu^-$ decay, a deviation of more than 1σ from the SM prediction is observed at the low and the high q^2 regions with $(\tilde{c}_{ql}^{(3)}, \tilde{c}'_Z)$ and $(\tilde{c}_{ql}^{(1)} + \tilde{c}_{ql}^{(3)}, \tilde{c}'_Z)$ NP couplings.

(vii) $\hat{K}_{1ss}$: In $\Lambda_b \to \Lambda^*(\to pK^-)\mu^+\mu^-$ channel, we observe a deviation of 3σ from the SM prediction in the presence of $(\tilde{c}_{ql}^{(3)}, \tilde{c}'_Z)$ and $(\tilde{c}_{ql}^{(1)} + \tilde{c}_{ql}^{(3)}, \tilde{c}'_Z)$ NP couplings at low q^2 region, whereas, it deviates more than 5σ at high q^2 region. Similarly, with $(\tilde{c}_{ql}^{(3)}, \tilde{c}'_Z)$ coupling, we observe a deviation of more than 1σ at the high q^2 region for the $\Lambda_b \to \Lambda(\to p\pi)\mu^+\mu^-$ decay mode.

TABLE XII. The branching ratio (BR), longitudinal polarization fraction F_L, lepton forward backward asymmetry $A_{\rm FB}$ and the ratio of branching ratio R_Λ for the $\Lambda_b \to \Lambda(\to p\pi)\mu^+\mu^-$ decay mode in case of few selected $2D$ NP scenarios.

		$\Lambda_b \to \Lambda(\to p\pi)\mu^+\mu^-$ decay (μ mode)			
SMEFT couplings		BR $\times 10^{-7}$	F_L	$A_{\rm FB}$	R_Λ
$(\tilde{c}_{ql}^{(3)}, \tilde{c}'_Z)$	1.1–6.0	0.628 [0.076, 2.650]	0.705 [0.104, 0.896]	0.070 [−0.274, −0.274]	0.807 [0.040, 2.958]
	$15.0 - q^2_{\rm max}$	1.934 [0.157, 10.021]	0.369 [0.278, 0.511]	0.050 [−0.403, 0.064]	0.523 [0.012, 4.074]
$(\tilde{c}_Z, \tilde{c}'_Z)$	1.1–6.0	0.636 [0.178, 1.989]	0.829 [0.656, 0.923]	0.030 [−0.099, 0.122]	0.817 [0.116, 2.405]
	$14.2 - q^2_{\rm max}$	2.739 [1.190, 8.196]	0.350 [0.282, 0.480]	0.012 [−0.410, 0.237]	0.741 [0.105, 3.197]
$(\tilde{c}_{ql}^{(1)} + \tilde{c}_{ql}^{(3)}, \tilde{c}'_Z)$	1.1–6.0	0.652 [0.076, 2.656]	0.708 [0.101, 0.896]	0.068 [−0.275, 0.246]	0.838 [0.040, 2.966]
	$15.0 - q^2_{\rm max}$	2.027 [0.158, 10.026]	0.368 [0.278, 0.510]	0.050 [−0.403, 0.064]	0.548 [0.012, 4.120]

TABLE XIII. Angular observables $\hat{K}_i$ for the $\Lambda_b \to \Lambda(\to p\pi)\mu^+\mu^-$ decay mode in case of few selected $2D$ NP scenarios.

		$\Lambda_b \to \Lambda(\to p\pi)\mu^+\mu^-$ decay							
SMEFT couplings	q^2 bin	$\hat{K}_{1c}$	$\hat{K}_{1cc}$	$\hat{K}_{1ss}$	$\hat{K}_{2c}$	$\hat{K}_{2cc}$	$\hat{K}_{2ss}$	$\hat{K}_{4sc}$	$\hat{K}_{4s}$
$(\tilde{c}_{ql}^{(3)}, \tilde{c}'_Z)$	1.1–6.0	0.046 [−0.183, 0.164]	0.148 [0.052, 0.448]	0.426 [0.276, 0.474]	−0.009 [−0.107, 0.119]	0.018 [−0.280, 0.062]	0.004 [−0.158, 0.027]	0.018 [−0.043, 0.067]	−0.084 [−0.213, 0.207]
	$15.0 - q^2_{\rm max}$	0.033 [−0.268, 0.043]	0.315 [0.245, 0.361]	0.342 [0.319, 0.378]	0.023 [−0.073, 0.212]	0.144 [−0.073, 0.212]	0.072 [−0.164, 0.156]	0.043 [−0.087, 0.071]	0.000 [−0.061, 0.051]
$(\tilde{c}_Z, \tilde{c}'_Z)$	1.1–6.0	0.020 [−0.066, 0.082]	0.085 [0.172, 0.038]	0.457 [0.414, 0.481]	0.012 [−0.028, 0.049]	0.023 [−0.080, 0.066]	0.009 [−0.040, 0.030]	0.020 [−0.062, 0.099]	0.098 [−0.151, 0.145]
	$15.0 - q^2_{\rm max}$	0.008 [−0.273, 0.158]	0.325 [0.260, 0.359]	0.338 [0.321, 0.370]	−0.132 [−0.189, 0.212]	0.013 [0.212, 0.043]	0.006 [−0.081, 0.021]	−0.000 [−0.060, 0.010]	0.197 [−0.200, 0.200]
$(\tilde{c}_{ql}^{(1)} + \tilde{c}_{ql}^{(3)}, \tilde{c}'_Z)$	1.1–6.0	0.046 [−0.183, 0.164]	0.146 [0.052, 0.052]	0.427 [0.275, 0.474]	−0.008 [−0.108, 0.119]	0.019 [−0.280, 0.063]	0.005 [−0.159, 0.028]	0.018 [−0.043, 0.067]	−0.083 [−0.213, 0.207]
	$15.0 - q^2_{\rm max}$	0.033 [−0.268, 0.043]	0.316 [0.245, 0.361]	0.342 [0.319, 0.378]	0.023 [−0.072, 0.212]	0.145 [−0.164, 0.156]	0.072 [−0.082, 0.078]	0.043 [−0.061, 0.051]	−0.000 [−0.177, 0.179]

(viii) $\hat{K}_{2c}$: For the $\Lambda_b \to \Lambda^*(\to pK^-)\mu^+\mu^-$ decay, we observe a deviation of more than 5σ and 10σ in case of all the NP scenarios at low and high q^2 regions, respectively. For the $\Lambda_b \to \Lambda(\to p\pi)\mu^+\mu^-$ decay channel, no significant deviation is observed at the low q^2 region. At the high q^2 region, however, it deviates more than 10σ in case of each NP scenarios.

(ix) $\hat{K}_{2cc}$: A deviation of around 3σ and 10σ is observed in the presence of $(\tilde{c}_{ql}^{(3)}, \tilde{c}'_Z)$ and $(\tilde{c}_{ql}^{(1)} + \tilde{c}_{ql}^{(3)}, \tilde{c}'_Z)$ couplings at the low and high q^2 regions, respectively for the $\Lambda_b \to \Lambda^*(\to pK^-)\mu^+\mu^-$ decay mode. Similarly, at the low and high q^2 regions, a deviation of more than 2σ and 10σ is observed in case of each NP scenarios for the $\Lambda_b \to \Lambda(\to p\pi)\mu^+\mu^-$ decay channel.

(x) $\hat{K}_{2ss}$: In $\Lambda_b \to \Lambda^*(\to pK^-)\mu^+\mu^-$ decay channel, a deviation of around 2σ from the SM prediction is observed in the presence of $(\tilde{c}_{ql}^{(3)}, \tilde{c}'_Z)$ coupling in the low q^2 region. However, in the high q^2 region, a deviation of more than 5σ is observed in the presence of the $(\tilde{c}_{ql}^{(3)}, \tilde{c}'_Z)$ and $(\tilde{c}_Z, \tilde{c}'_Z)$ couplings. Similarly, for the $\Lambda_b \to \Lambda(\to p\pi)\mu^+\mu^-$ decay channel, a deviation of more than 2σ and 10σ is observed in each NP scenarios at the low and high q^2 regions, respectively.

(xi) $\hat{K}_{4ss}$: For the $\Lambda_b \to \Lambda^*(\to pK^-)\mu^+\mu^-$ decay channel, no significant deviation is observed in the low q^2 region. However, a deviation of more than 4σ and 10σ is observed in the presence of $(\tilde{c}_{ql}^{(3)}, \tilde{c}'_Z)$, $(\tilde{c}_Z, \tilde{c}'_Z)$ and $(\tilde{c}_{ql}^{(1)} + \tilde{c}_{ql}^{(3)}, \tilde{c}'_Z)$ NP couplings at the high q^2 region.

(xii) $\hat{K}_{5s}$: There is a deviation of more than 4σ in the low q^2 region for the $\Lambda_b \to \Lambda^*(\to pK^-)\mu^+\mu^-$ decay channel in case of all the NP scenarios. Moreover, at the high q^2 region, more than 5σ deviation is observed in the presence of $(\tilde{c}_{ql}^{(3)}, \tilde{c}'_Z)$ and $(\tilde{c}_Z, \tilde{c}'_Z)$ couplings.

(xiii) $\hat{K}_{4sc}$: In the low q^2 region, no significant deviation is observed in $\hat{K}_{4sc}$ for the $\Lambda_b \to \Lambda(\to p\pi)\mu^+\mu^-$ decay mode. However, in the high q^2 region, a deviation of more than 5σ is observed in the presence of $(\tilde{c}_{ql}^{(3)}, \tilde{c}'_Z)$, $(\tilde{c}_Z, \tilde{c}'_Z)$, and $(\tilde{c}_{ql}^{(1)} + \tilde{c}_{ql}^{(3)}, \tilde{c}'_Z)$ NP couplings.

(xiv) $\hat{K}_{4s}$: For the $\Lambda_b \to \Lambda^*(\to pK^-)\mu^+\mu^-$ decay channel, a deviation of around 1σ is observed in the low q^2 region with $(\tilde{c}_{ql}^{(3)}, \tilde{c}'_Z)$ and $(\tilde{c}_{ql}^{(1)} + \tilde{c}_{ql}^{(3)}, \tilde{c}'_Z)$ NP couplings. However, in the high q^2 region, $\hat{K}_{4s}$ deviates from the SM prediction by more than 5σ in each NP scenarios.

In Figs. 2 and 3, we display several q^2 dependent observables pertaining to $\Lambda_b \to \Lambda^*(\to pK^-)\mu^+\mu^-$ and $\Lambda_b \to \Lambda(\to p\pi)\mu^+\mu^-$ decay modes in the SM and in few selected NP scenarios, namely $(\tilde{c}_{ql}^{(3)}, \tilde{c}'_Z)$, $(\tilde{c}_Z, \tilde{c}'_Z)$, and $(\tilde{c}_{ql}^{(1)} + \tilde{c}_{ql}^{(3)}, \tilde{c}'_Z)$, respectively. The SM central line and the corresponding uncertainty band obtained at 95% C.L. are shown with blue color, whereas, the effects of $(\tilde{c}_{ql}^{(3)}, \tilde{c}'_Z)$, $(\tilde{c}_Z, \tilde{c}'_Z)$ and $(\tilde{c}_{ql}^{(1)} + \tilde{c}_{ql}^{(3)}, \tilde{c}'_Z)$ NP couplings are shown with green, orange and red color respectively. Our main observations are as follows.

(i) $\boldsymbol{dB/dq^2(q^2)}$: The differential branching ratio for $\Lambda_b \to \Lambda^*(\to pK^-)\mu^+\mu^-$ and $\Lambda_b \to \Lambda(\to p\pi)\mu^+\mu^-$ decays is reduced at all q^2 in case of most of the NP scenarios. In $\Lambda_b \to \Lambda(\to p\pi)\mu^+\mu^-$ decays, the differential branching ratio is enhanced with $(\tilde{c}_Z, \tilde{c}'_Z)$ NP coupling. All the NP scenarios are distinguishable from the SM prediction at more than 1σ in the

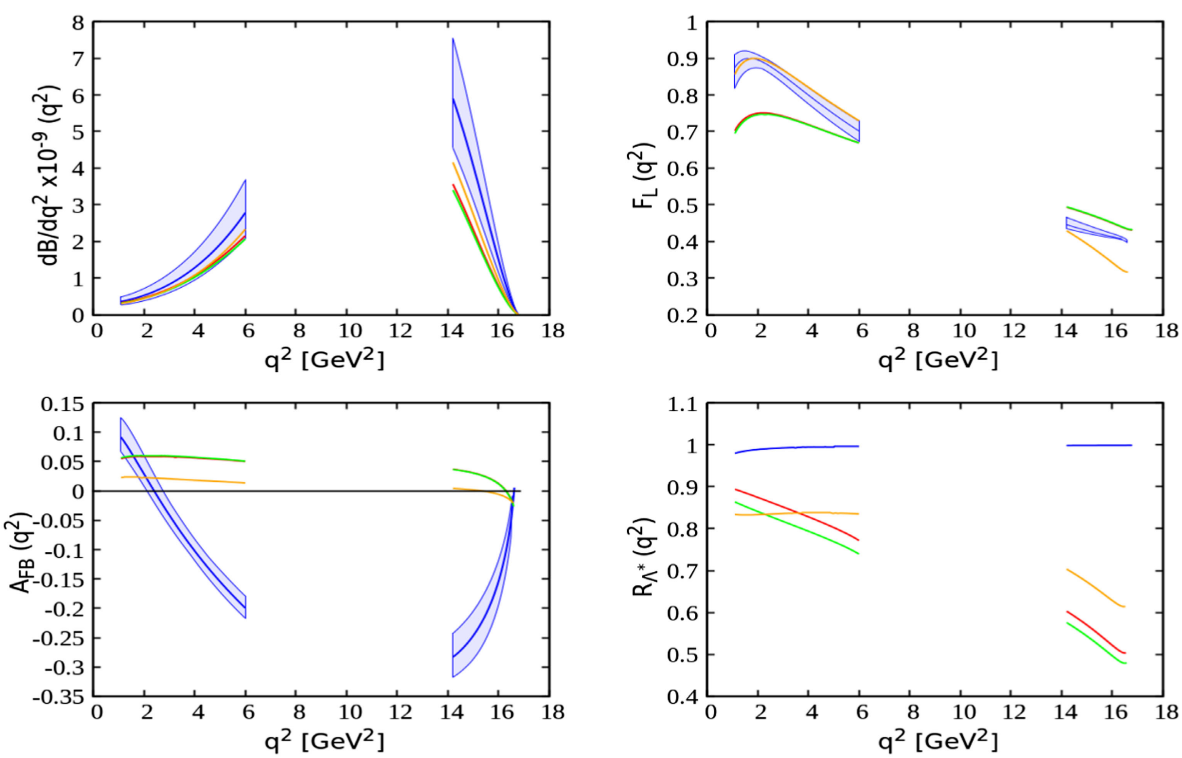

FIG. 2. q^2 dependence of differential branching ratio $dB/dq^2(q^2)$, longitudinal polarization fraction $F_L(q^2)$, lepton forward backward asymmetry $A_{FB}^l(q^2)$ and the ratio of branching ratio $R_{\Lambda^*}(q^2)$ for the $\Lambda_b \to \Lambda^*(\to pK^-)\mu^+\mu^-$ decay mode. The SM central line and the corresponding error band is shown with blue. The green, orange, and red lines correspond to the best fit values of $(\tilde{c}_{ql}^{(3)}, \tilde{c}'_Z)$, $(\tilde{c}_Z, \tilde{c}'_Z)$, and $(\tilde{c}_{ql}^{(1)} + \tilde{c}_{ql}^{(3)}, \tilde{c}'_Z)$, respectively.

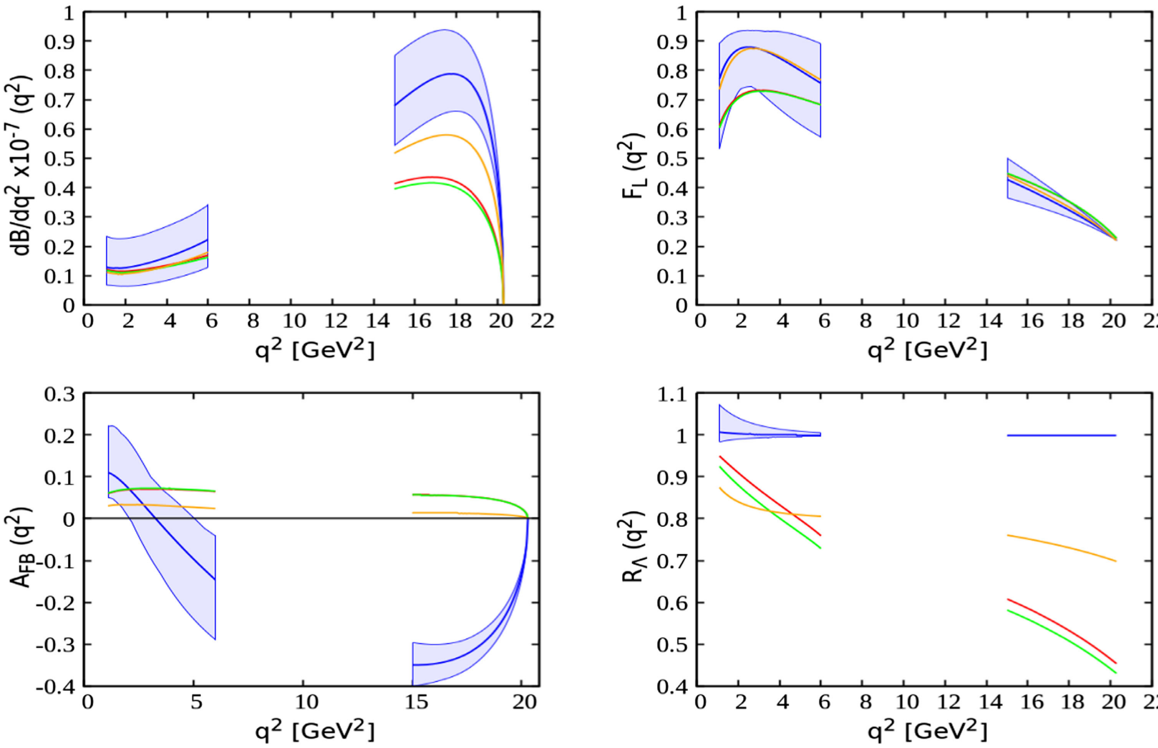

FIG. 3. q^2 dependence of differential branching ratio $dB/dq^2(q^2)$, longitudinal polarization fraction $F_L(q^2)$, lepton forward backward asymmetry $A^l_{\rm FB}(q^2)$ and the ratio of branching ratio $R_{\Lambda^*}(q^2)$ for the $\Lambda_b \to \Lambda(\to p\pi)\mu^+\mu^-$ decay mode. The SM central line and the corresponding error band is shown with blue. The green, orange and red lines correspond to the best fit values of $(\tilde{c}^{(3)}_{ql}, \tilde{c}'_Z)$, $(\tilde{c}_Z, \tilde{c}'_Z)$, and $(\tilde{c}^{(1)}_{ql} + \tilde{c}^{(3)}_{ql}, \tilde{c}'_Z)$, respectively.

high q^2 region. In the low q^2 region, however, it lies within the SM error band. The deviation from the SM prediction is more pronounced in case of $(\tilde{c}^{(3)}_{ql}, \tilde{c}'_Z)$ NP scenario.

(ii) $\boldsymbol{F_L(q^2)}$: For the $\Lambda_b \to \Lambda^*(\to pK^-)\mu^+\mu^-$ decay channel, deviation in $F_L(q^2)$ from the SM prediction is more pronounced in case of $(\tilde{c}^{(3)}_{ql}, \tilde{c}'_Z)$ and $(\tilde{c}^{(1)}_{ql} + \tilde{c}^{(3)}_{ql}, \tilde{c}'_Z)$ NP scenarios in the low q^2 region. In the high q^2 region, the deviation from SM prediction is more prominent in case of $(\tilde{c}^{(3)}_{ql}, \tilde{c}'_Z)$ and $(\tilde{c}_Z, \tilde{c}'_Z)$ NP scenarios and they are clearly distinguishable from the SM at more than 2σ significance. In the case of $\Lambda_b \to \Lambda(\to p\pi)\mu^+\mu^-$ decay, although a slight deviation is observed in case of $(\tilde{c}^{(3)}_{ql}, \tilde{c}'_Z)$ NP scenario, it, however, is indistinguishable from the SM prediction.

(iii) $\boldsymbol{A_{FB}(q^2)}$: For the $\Lambda_b \to \Lambda^*(\to pK^-)\mu^+\mu^-$ decay channel, a significant deviation from the SM prediction is observed in $A_{\rm FB}(q^2)$ in case of all the NP scenarios and they are clearly distinguishable from the SM at more than 6σ at low and high q^2 regions. In the SM, we observe the zero crossing point of $A_{\rm FB}$ at $q^2 = 2.4 \pm 0.6$ GeV^2 and at $q^2 = 16.6 \pm 0.1$ GeV^2, respectively. With NP, there is no zero crossing of $A_{\rm FB}$ at low q^2 region. However, at the high q^2 region, we observe the zero crossing point at $q^2 = 15.3$ GeV^2 and $q^2 = 16.3$ GeV^2 with $(\tilde{c}_Z, \tilde{c}'_Z)$, $(\tilde{c}^{(3)}_{ql}, \tilde{c}'_Z)$, and $(\tilde{c}^{(1)}_{ql} + \tilde{c}^{(3)}_{ql}, \tilde{c}'_Z)$ NP couplings, respectively. For $\Lambda_b \to \Lambda(\to p\pi)\mu^+\mu^-$ decay, in the low q^2 region, a slight deviation in $A_{\rm FB}$ is observed with all the NP scenarios but they are indistinguishable from the SM prediction. However, at high q^2 region, the deviation observed is quite significant and all the NP scenarios are distinguishable from the SM prediction at more than 10σ. In the SM, a zero crossing point of $A_{\rm FB}$ is observed at $q^2 = 3.3 \pm 1.5$ GeV^2. However, no zero crossing point is observed with NP couplings for this decay channel.

(iv) $\boldsymbol{R_{\Lambda^{(*)}}(q^2)}$: The ratio of branching fraction $R_{\Lambda^{(*)}}(q^2)$ shows significant deviation in case of all the NP scenarios and it is clearly distinguishable from the SM prediction at more than 10σ significance at both low and high q^2 regions.

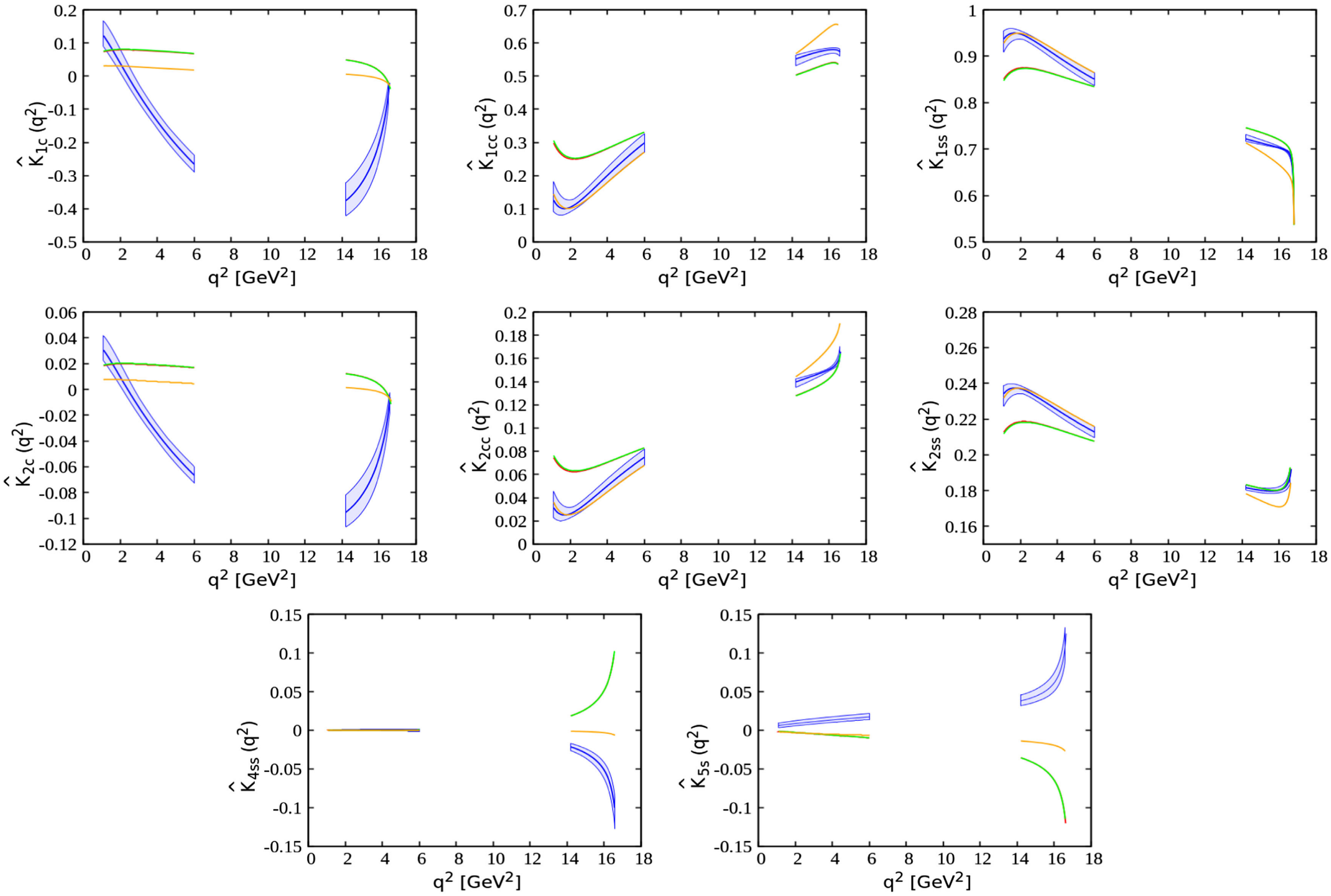

FIG. 4. q^2 dependence of several $\hat{K}$ observables for the $\Lambda_b \to \Lambda^*(\to pK^-)\mu^+\mu^-$ decay mode. The SM central line and the corresponding error band is shown with blue. The green, orange and red lines correspond to the best fit values of $(\tilde{c}_{ql}^{(3)}, \tilde{c}'_Z)$, $(\tilde{c}_Z, \tilde{c}'_Z)$, and $(\tilde{c}_{ql}^{(1)} + \tilde{c}_{ql}^{(3)}, \tilde{c}'_Z)$, respectively.

In Figs. 4 and 5, we display the NP sensitivities of several $\hat{K}_i$ observables for the $\Lambda_b \to \Lambda^*(\to pK^-)\mu^+\mu^-$ and $\Lambda_b \to \Lambda(\to p\pi)\mu^+\mu^-$ decay modes in the low and high q^2 regions. The SM central line and the error band is shown with blue. The green, orange and red lines correspond to NP contributions coming from the best fit values of $(\tilde{c}_{ql}^{(3)}, \tilde{c}'_Z)$, $(\tilde{c}_Z, \tilde{c}'_Z)$, and $(\tilde{c}_{ql}^{(1)} + \tilde{c}_{ql}^{(3)}, \tilde{c}'_Z)$ NP couplings of Table VII.

Although deviation from the SM prediction in the $\hat{K}_i$ observables is observed in case of all the NP scenarios, it is, however, more pronounced in case of $(\tilde{c}_{ql}^{(3)}, \tilde{c}'_Z)$ and $(\tilde{c}_Z, \tilde{c}'_Z)$ NP scenarios. For the $\Lambda_b \to \Lambda^*(\to pK^-)\mu^+\mu^-$ channel, it is observed that, irrespective of the NP contribution, the ratios $\hat{K}_{1c}/\hat{K}_{2c}$, $\hat{K}_{1cc}/\hat{K}_{2cc}$, and $\hat{K}_{1ss}/\hat{K}_{2ss}$ remain independent of both short distance and long distance physics. For $\hat{K}_{1c}$ and $\hat{K}_{2c}$ the dependence on the new physics follow the same pattern as in $A_{\rm FB}$. Similarly, for $\hat{K}_{1cc}$ and $\hat{K}_{2cc}$, the dependence on the new physics follow the same pattern as in F_L. For the $\Lambda_b \to \Lambda(\to p\pi)\mu^+\mu^-$ channel, NP dependence of $\hat{K}_{1c}$ follows the same pattern as in $A_{\rm FB}$. Similarly, for $\hat{K}_{1cc}$ and $\hat{K}_{1ss}$, the NP dependence is quite similar to that of F_L. Moreover, variation of $\hat{K}_{2cc}$ and $\hat{K}_{2ss}$ as a function of q^2 looks quite similar in case of $\Lambda_b \to \Lambda(\to p\pi)\mu^+\mu^-$ decay channel. We observe that deviation from the SM prediction is more pronounced in case of $(\tilde{c}_{ql}^{(3)}, \tilde{c}'_Z)$ and $(\tilde{c}_Z, \tilde{c}'_Z)$ NP scenarios.

We now proceed to discuss the effects of NP in $\Lambda_b \to \Lambda^*(\to pK^-)\nu\bar{\nu}$ and $\Lambda_b \to \Lambda(\to p\pi)\nu\bar{\nu}$ decay observables.

E. Effects of SMEFT coefficients in $\Lambda_b \to \Lambda^*(\to pK^-)\nu\bar{\nu}$ and $\Lambda_b \to \Lambda(\to p\pi)\nu\bar{\nu}$ decay observables

Study of rare decays mediated via $b \to s\nu\bar{\nu}$ quark level transition can, in principle, provide complementary information regarding NP in $b \to s\ell^+\ell^-$ transition decays. In this connection, we wish to explore the effects of NP in $b \to s\ell^+\ell^-$ transition decays on several observables pertaining to $\Lambda_b \to \Lambda^*(\to pK^-)\nu\bar{\nu}$ and $\Lambda_b \to \Lambda(\to p\pi)\nu\bar{\nu}$ decay modes. We consider three NP scenarios such as $(\tilde{c}_{ql}^{(3)}, \tilde{c}'_Z)$, $(\tilde{c}_Z, \tilde{c}'_Z)$, and $(\tilde{c}_{ql}^{(1)} + \tilde{c}_{ql}^{(3)}, \tilde{c}'_Z)$ from Table VII that

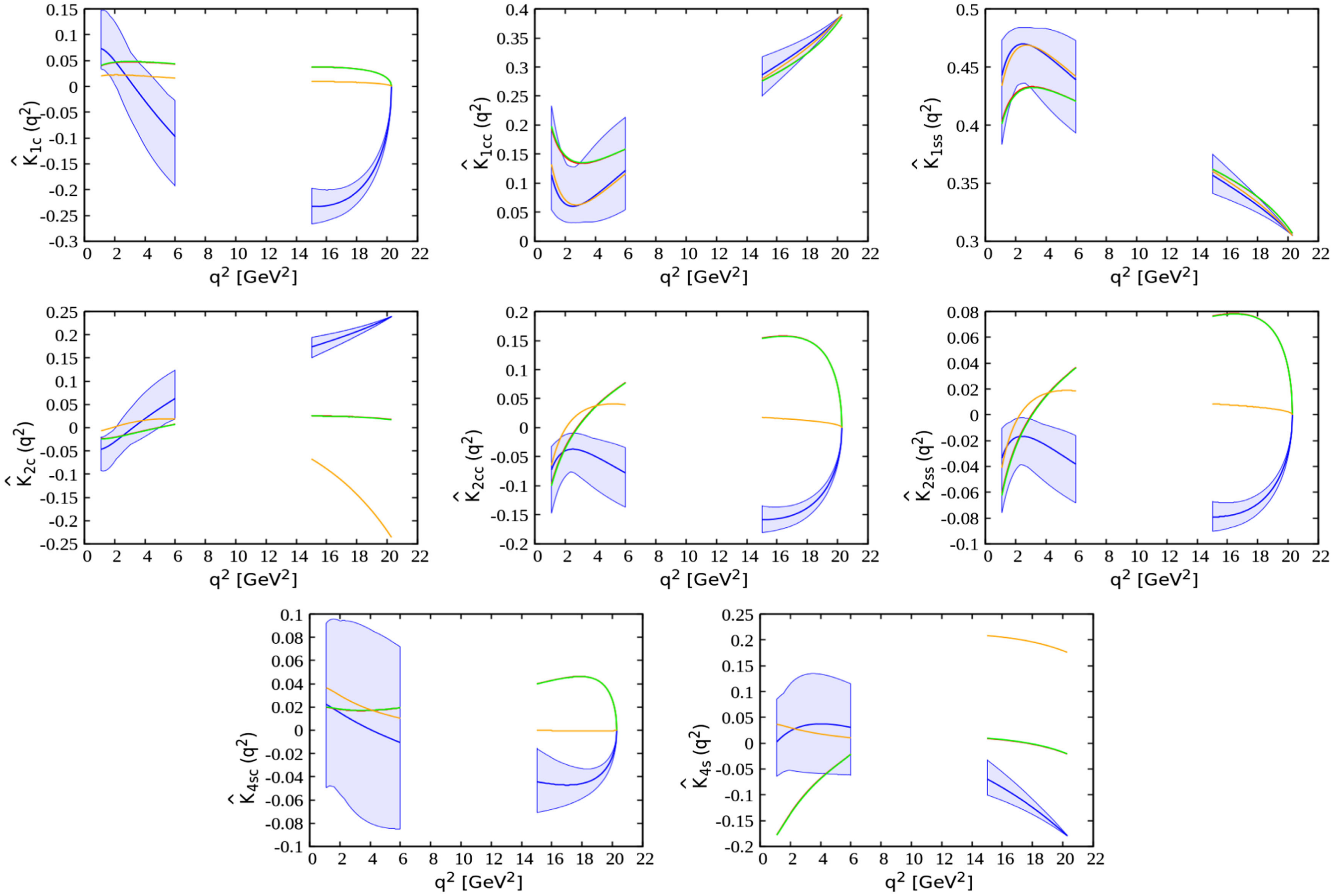

FIG. 5. q^2 dependence of several K observables for the $\Lambda_b \to \Lambda(\to p\pi)\mu^+\mu^-$ decay mode. The SM central line and the corresponding error band is shown with blue. The green, orange, and red lines correspond to the best fit values of $(\tilde{c}_{ql}^{(3)}, \tilde{c}'_Z)$, $(\tilde{c}_Z, \tilde{c}'_Z)$, and $(\tilde{c}_{ql}^{(1)} + \tilde{c}_{ql}^{(3)}, \tilde{c}'_Z)$, respectively.

best explain the anomalies present in the $b \to s\ell^+\ell^-$ data. Effect of these NP couplings on $\Lambda_b \to \Lambda^*(\to pK^-)\nu\bar{\nu}$ and $\Lambda_b \to \Lambda(\to p\pi)\nu\bar{\nu}$ decay observables are listed in Table XIV.

Our main observations are as follows.

(i) **BR**: In the $\Lambda_b \to \Lambda^*(\to pK^-)\nu\bar{\nu}$ decay channel, branching ratio deviates more than 1σ from the SM prediction in the presence of $(\tilde{c}_Z, \tilde{c}'_Z)$ and $(\tilde{c}_{ql}^{(1)} + \tilde{c}_{ql}^{(3)}, \tilde{c}'_Z)$ NP couplings. Similarly, in the $\Lambda_b \to \Lambda(\to p\pi)\nu\bar{\nu}$ decay channel, the branching ratio deviates more than 2σ in the presence of $(\tilde{c}_{ql}^{(3)}, \tilde{c}'_Z)$ and $(\tilde{c}_Z, \tilde{c}'_Z)$ NP couplings.

(ii) $\boldsymbol{F_L}$: For the $\Lambda_b \to \Lambda^*(\to pK^-)\nu\bar{\nu}$ decay mode, F_L shows 2σ, 3.3σ, and 4σ deviations from the SM prediction in the presence of $(\tilde{c}_{ql}^{(1)} + \tilde{c}_{ql}^{(3)}, \tilde{c}'_Z)$,

TABLE XIV. The branching ratio (BR) and longitudinal polarization fraction F_L for the $\Lambda_b \to \Lambda^*(\to pK^-)\nu\bar{\nu}$ and $\Lambda_b \to \Lambda(\to p\pi)\nu\bar{\nu}$ decay modes in case of few selected $2D$ NP scenarios.

	$\Lambda_b \to \Lambda^*(\to pK^-)\nu\bar{\nu}$ decay		$\Lambda_b \to \Lambda(\to p\pi)\nu\bar{\nu}$ decay	
SMEFT couplings	BR $\times 10^{-6}$	F_L	BR $\times 10^{-6}$	F_L
$(\tilde{c}_{ql}^{(3)}, \tilde{c}'_Z)$	1.205 [−0.001, 3.931]	0.717 [0.507, 0.731]	1.007 [0.001, 4.243]	0.595 [0.318, 0.710]
$(\tilde{c}_Z, \tilde{c}'_Z)$	0.834 [0.006, 3.288]	0.716 [0.506, 0.730]	0.689 [0.000, 3.624]	0.581 [0.333, 0.721]
$(\tilde{c}_{ql}^{(1)} + \tilde{c}_{ql}^{(3)}, \tilde{c}'_Z)$	2.053 [0.006, 3.288]	0.669 [0.506, 0.730]	2.060 [1.327, 4.650]	0.624 [0.330, 0.709]

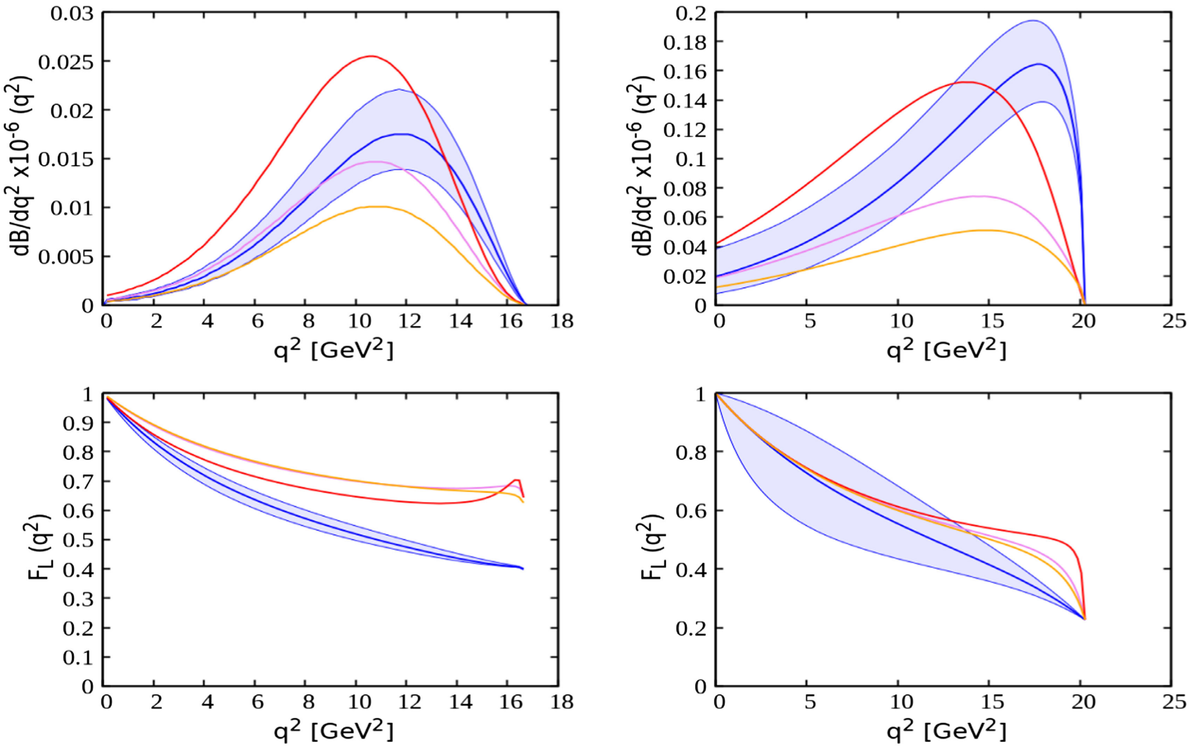

FIG. 6. q^2 dependence of differential branching ratio $dB/dq^2(q^2)$ and longitudinal polarization fraction $F_L(q^2)$ for the $\Lambda_b \to \Lambda^*(\to pK^-)\nu\bar{\nu}$ and $\Lambda_b \to \Lambda(\to p\pi)\nu\bar{\nu}$ decay mode. The SM central line and the corresponding error band is shown with blue. The violet, orange, and red lines correspond to the best fit values of $(\tilde{c}_{ql}^{(3)}, \tilde{c}_Z')$, $(\tilde{c}_Z, \tilde{c}_Z')$, and $(\tilde{c}_{ql}^{(1)} + \tilde{c}_{ql}^{(3)}, \tilde{c}_Z')$, respectively.

$(\tilde{c}_{ql}^{(3)}, \tilde{c}_Z')$, and $(\tilde{c}_Z, \tilde{c}_Z')$ NP couplings, respectively. Similarly, for the $\Lambda_b \to \Lambda(\to p\pi)\nu\bar{\nu}$ decay mode, F_L shows deviations of around 1σ and 2σ from the SM prediction in presence of these NP couplings.

In Fig. 6, we display differential branching ratio dB/dq^2 and longitudinal polarization fraction $F_L(q^2)$ pertaining to $\Lambda_b \to \Lambda^{(*)}\nu\bar{\nu}$ decay modes in the SM and in case of $(\tilde{c}_{ql}^{(3)}, \tilde{c}_Z')$, $(\tilde{c}_Z, \tilde{c}_Z')$, and $(\tilde{c}_{ql}^{(1)} + \tilde{c}_{ql}^{(3)}, \tilde{c}_Z')$ NP scenarios. The SM central line and the corresponding uncertainty band obtained at 95% C.L. are shown with blue color, whereas, the effects of $(\tilde{c}_{ql}^{(3)}, \tilde{c}_Z')$, $(\tilde{c}_Z, \tilde{c}_Z')$, and $(\tilde{c}_{ql}^{(1)} + \tilde{c}_{ql}^{(3)}, \tilde{c}_Z')$ are represented by violet, orange, and red color respectively. Our observations are as follows.

(i) ***dB/dq*²(*q*²)**: The differential branching ratio for $\Lambda_b \to \Lambda^*(\to pK^-)\nu\bar{\nu}$ decays is enhanced at all q^2 below $q^2 < 12$ GeV^2, whereas, it is reduced at the high q^2 region in case of $(\tilde{c}_{ql}^{(1)} + \tilde{c}_{ql}^{(3)}, \tilde{c}_Z')$ NP scenario. With $(\tilde{c}_{ql}^{(3)}, \tilde{c}_Z')$ NP coupling, the differential branching ratio lies within the SM error band except at $q^2 > 12$ GeV^2. Similarly, with $(\tilde{c}_Z, \tilde{c}_Z')$ NP coupling, it is reduced at all values of q^2. The deviation from the SM prediction is more pronounced in case of $(\tilde{c}_{ql}^{(1)} + \tilde{c}_{ql}^{(3)}, \tilde{c}_Z')$ and $(\tilde{c}_Z, \tilde{c}_Z')$ NP scenarios and they are clearly distinguishable from the SM prediction at more than 2σ. It should be noted that, in all the NP scenarios, the peak of the q^2 distribution appears at slightly lower value of q^2 than in the SM.

In case of $\Lambda_b \to \Lambda(\to p\pi)\nu\bar{\nu}$ decays, the differential branching ratio is slightly enhanced at all q^2 below $q^2 < 13$ GeV^2 whereas, it is reduced at the high q^2 region in case of $(\tilde{c}_{ql}^{(1)} + \tilde{c}_{ql}^{(3)}, \tilde{c}_Z')$ NP scenario. However, it is reduced at all q^2 with $(\tilde{c}_{ql}^{(3)}, \tilde{c}_Z')$ and $(\tilde{c}_Z, \tilde{c}_Z')$ NP couplings. The deviation from the SM prediction is more pronounced in case of $(\tilde{c}_{ql}^{(3)}, \tilde{c}_Z')$ and $(\tilde{c}_Z, \tilde{c}_Z')$ NP scenarios and they are clearly distinguishable from the SM prediction at more than 3σ. Moreover, similar to $\Lambda_b \to \Lambda^*(\to pK^-)\nu\bar{\nu}$ decays, the peak of the distribution appears at slightly lower value of q^2 than in the SM.

(ii) ***F*$_L$(*q*²)**: For both the decay modes, the longitudinal polarization fraction $F_L(q^2)$ is enhanced at all q^2 in case of all the NP scenarios. The deviation from the SM prediction observed in the high q^2 region is quite significant and they are clearly distinguishable from the SM prediction at more than 3σ. The deviation from the SM prediction is more pronounced in case of $(\tilde{c}_Z, \tilde{c}_Z')$ NP scenario.

IV. CONCLUSION

In light of anomalies observed in various $b \to s\ell^+\ell^-$ quark-level transition decays, we perform an in-depth angular analysis of baryonic $\Lambda_b \to \Lambda^*(\to pK^-) \times (\mu^+\mu^-, \nu\bar{\nu})$ and $\Lambda_b \to \Lambda(\to p\pi)(\mu^+\mu^-, \nu\bar{\nu})$ decays mediated via $b \to s\ell^+\ell^-$ and $b \to s\nu\bar{\nu}$ quark level transition. Our main aim of this study is to explore the connections between $b \to s\ell^+\ell^-$ and $b \to s\nu\bar{\nu}$ quark level transition decays in a model independent way. In this context, we use the standard model effective field theory formalism with dimension six operators that can, in principle, provide correlated NP effects in these decay modes. For the $\Lambda_b \to \Lambda^*$ form factors we use the values obtained from MCN, whereas, for the $\Lambda_b \to \Lambda$ form factors, we use the recent results obtained from LQCD approach. We construct several NP scenarios based on NP contributions from single operators as well as from two different operators and try to find the scenario that best explains the anomalies present in $b \to s\ell^+\ell^-$ transition decays. To find the best fit values of the SMEFT coefficients, we perform a naive χ^2 analysis with the $b \to s\ell^+\ell^-$ data. We include total eight measurements in our χ^2 fit. It should, however, be mentioned that, in our χ^2 fit, we have not included the latest $R_K^{(*)}$ measurement from LHCb. It is observed that the $2D$ scenarios provide better fit to the $b \to s\ell^+\ell^-$ data than the $1D$ scenarios. More specifically, we get much better fit with $(\tilde{c}_{ql}^{(1)}, \tilde{c}'_Z)$, $(\tilde{c}_{ql}^{(3)}, \tilde{c}'_Z)$, $(\tilde{c}_Z, \tilde{c}'_Z)$, and $(\tilde{c}_{ql}^{(1)} + \tilde{c}_{ql}^{(3)}, \tilde{c}'_Z)$ NP scenarios. The pull_{SM} for these $2D$ scenarios are comparatively larger than any other scenarios. Next we check the compatibility of our fit results with the measured values of $\mathcal{B}(B \to K^{(*)}\nu\bar{\nu})$. It is observed that the allowed ranges of $\mathcal{B}(B \to K\nu\bar{\nu})$ and $\mathcal{B}(B \to K^*\nu\bar{\nu})$ obtained with $(\tilde{c}_{ql}^{(3)}, \tilde{c}'_Z)$ and $(\tilde{c}_Z, \tilde{c}'_Z)$ SMEFT scenarios are compatible with the experimental upper bound. In case of $(\tilde{c}_{ql}^{(1)}, \tilde{c}'_Z)$ and $(\tilde{c}_{ql}^{(1)} + \tilde{c}_{ql}^{(3)}, \tilde{c}'_Z)$ NP scenarios, although the best fit value does not simultaneously satisfy the experimental upper bound, there still exist some NP parameter space that can, in principle, satisfy both the constraint.

A brief summary of our results are as follows.

(i) The differential branching ratio for the $\Lambda_b \to \Lambda^*(\to pK^-)\mu^+\mu^-$ and $\Lambda_b \to \Lambda(\to p\pi)\mu^+\mu^-$ decays deviates from the SM prediction in case of all the NP scenarios and they are distinguishable from the SM prediction at more than 1σ in the high q^2 region. Similarly, $A_{\text{FB}}(q^2)$ deviates significantly from the SM prediction in case of all the NP scenarios. For the $\Lambda_b \to \Lambda^*(\to pK^-)\mu^+\mu^-$ decay mode, the zero crossing point of $A_{\text{FB}}(q^2)$ at $q^2 = 15.3\ \text{GeV}^2$ and $q^2 = 16.3\ \text{GeV}^2$ with $(\tilde{c}_Z, \tilde{c}'_Z)$, $(\tilde{c}_{ql}^{(1),(3)}, \tilde{c}'_Z)$ and $(\tilde{c}_{ql}^{(1)} + \tilde{c}_{ql}^{(3)}, \tilde{c}'_Z)$ NP couplings are clearly distinguishable from the SM zero crossing point at $q^2 = 16.6 \pm 0.1\ \text{GeV}^2$. For the $\Lambda_b \to \Lambda(\to p\pi)\mu^+\mu^-$ decays, although there is a zero crossing point at $q^2 = 3.3 \pm 1.5\ \text{GeV}^2$, no zero crossing point is observed with NP couplings for this decay channel. Moreover, the ratio of branching ratio $R_{\Lambda^{(*)}}$ deviates significantly from the SM prediction in case of all the NP scenarios.

(ii) In case of $\Lambda_b \to \Lambda^*(\to pK^-)\nu\bar{\nu}$ decay, the deviation from the SM prediction in the differential branching ratio is more pronounced in case of $(\tilde{c}_{ql}^{(1)} + \tilde{c}_{ql}^{(3)}, \tilde{c}'_Z)$ and $(\tilde{c}_Z, \tilde{c}'_Z)$ NP scenarios and they are clearly distinguishable from the SM prediction at more than 2σ. In case of $\Lambda_b \to \Lambda(\to p\pi)\nu\bar{\nu}$ decays, The deviation from the SM prediction is more pronounced in case of $(\tilde{c}_{ql}^{(3)}, \tilde{c}'_Z)$ and $(\tilde{c}_Z, \tilde{c}'_Z)$ NP scenarios and they are clearly distinguishable from the SM prediction at more than 3σ. Similarly, F_L deviates significantly from the SM prediction in the high q^2 region and it is clearly distinguishable from the SM prediction at more than 3σ.

Study of $\Lambda_b \to \Lambda^*(\to pK^-)(\mu^+\mu^-, \nu\bar{\nu})$ and $\Lambda_b \to \Lambda(\to p\pi)(\mu^+\mu^-, \nu\bar{\nu})$ mediated via $b \to s\ell^+\ell^-$ and $b \to s\nu\bar{\nu}$ transition decays can be valuable in understanding the anomalies observed in B meson decays. Our analysis can be further improved once more precise data on the $\Lambda_b \to \Lambda^*$ form factor is available from LQCD. Moreover, more precise data on $\mathcal{B}(B \to K\nu\bar{\nu})$ and $\mathcal{B}(B \to K^*\nu\bar{\nu})$ in future, can, in principle, put severe constraint on several NP scenarios.

ACKNOWLEDGMENTS

We would like to express our gratitude to N. Rajeev for insightful and engaging discussions related to the topic addressed in this article. We would also like to thank Diganta Das, Jaydeb Das, and Stefan Meinel for their helpful exchanges regarding $\Lambda_b \to \Lambda^*$ transition form factors.

APPENDIX: EXPRESSIONS FOR THE $\Lambda_b \to \Lambda \times (\to p\pi)\nu\bar{\nu}$ AND $\Lambda_b \to \Lambda^*(\to pK^-)\nu\bar{\nu}$ DECAYS

The expressions of four-fold angular distribution for the charged leptons provided in Eqs. (9) and (14) can be used for the dineutrino modes as well. However, it is crucial to note that the angular coefficients K_i, written in terms of the tranversity amplitudes, will differ significantly in case of dineutrino channels. One can, in principle, obtain the transversity amplitudes for the $b \to s\nu\nu$ process from the $b \to s\ell\ell$ decay process. Let us start from the effective Hamiltonian ($\mathcal{H}_{\text{eff}}$) so that a clear connection between $b \to s\ell\ell$ and $b \to s\nu\nu$ processes can be made.

For the $b \to s\ell^+\ell^-$ transition decays, the effective Hamiltonian can be written as

$$\mathcal{H}_{\rm eff} = -\frac{4G_F}{\sqrt{2}} V_{tb} V_{ts}^* \frac{e^2}{16\pi^2} \Big[C_9 (\bar{s}\gamma_\mu P_L b)(\bar{l}\gamma^\mu l) + C_{9'} (\bar{s}\gamma_\mu P_R b)(\bar{l}\gamma^\mu l) + C_{10} (\bar{s}\gamma_\mu P_L b)(\bar{l}\gamma^\mu \gamma_5 l) + C_{10'} (\bar{s}\gamma_\mu P_R b)(\bar{l}\gamma^\mu \gamma_5 l) \Big] + {\rm H.c.} \quad ({\rm A1})$$

Similarly for the $b \to s\nu\bar{\nu}$ transition decays, it can be written as

$$\begin{aligned}\mathcal{H}_{\rm eff} &= -\frac{4G_F}{\sqrt{2}} V_{tb} V_{ts}^* \frac{e^2}{16\pi^2} \Big[C_L (\bar{s}\gamma_\mu P_L b)(\bar{\nu}\gamma^\mu (1-\gamma_5)\nu) + C_R (\bar{s}\gamma_\mu P_R b)(\bar{\nu}\gamma^\mu (1-\gamma_5)\nu) \Big] + {\rm H.c.}, \\ &= -\frac{4G_F}{\sqrt{2}} V_{tb} V_{ts}^* \frac{e^2}{16\pi^2} \Big[C_L (\bar{s}\gamma_\mu P_L b)(\bar{\nu}\gamma^\mu \nu) - C_L (\bar{s}\gamma_\mu P_L b)(\bar{\nu}\gamma_5\gamma^\mu \nu) + C_R (\bar{s}\gamma_\mu P_R b)(\bar{\nu}\gamma^\mu \nu) - C_R (\bar{s}\gamma_\mu P_R b)(\bar{\nu}\gamma_5\gamma^\mu \nu) \Big] + {\rm H.c.}\end{aligned} \quad ({\rm A2})$$

Comparing Eqs. (A1) and (A2), one can establish a relation between the $b \to s\ell^+\ell^-$ and $b \to s\nu\bar{\nu}$ decays as follows

$$C_9 = C_L \quad C_{10} = -C_L \quad C_9' = C_R \quad C_{10}' = -C_R. \quad ({\rm A3})$$

It is also evident from Eqs. (10) and (15) that the terms involving $K'_{\{...\}}$ and $K''_{\{...\}}$ will not contribute to the dineutrino modes as the lepton mass will be zero for $\nu\bar{\nu}$ channels. The transversity amplitudes for the dineutrino channels can be derived directly from the expressions of the $b \to s\mu^+\mu^-$ decay by using Eq. (A3) and setting the lepton mass to zero ($m_l = 0$). This will allow us to obtain the equation for $\Lambda_b \to \Lambda^{(*)}\nu\bar{\nu}$ decays from the $\Lambda_b \to \Lambda^{(*)}\mu^+\mu^-$ decay channels. All the expressions for the transversity amplitudes pertaining to $\Lambda_b \to \Lambda^{(*)}\nu\bar{\nu}$ decays are provided below.

For the $\Lambda_b \to \Lambda^*(\to pK^-)\nu\bar{\nu}$ decay, the transversity amplitudes can be expressed as

$$B^L_{\perp_1} = 2\sqrt{2} N f_g^V \sqrt{s_+} \mathcal{C}^L_{\rm VA+} (C_L + C_R), \quad ({\rm A4})$$

$$B^L_{\parallel_1} = 2\sqrt{2} N f_g^A \sqrt{s_-} (C_L - C_R) \quad ({\rm A5})$$

$$A^L_{\perp_0} = -2\sqrt{2} N f_0^V \frac{(m_{\Lambda_b} + m_{\Lambda^*})}{\sqrt{q^2}} \frac{s_-\sqrt{s_+}}{\sqrt{6} m_{\Lambda^*}} (C_L + C_R), \quad ({\rm A6})$$

$$A^L_{\parallel_0} = 2\sqrt{2} N f_0^A \frac{(m_{\Lambda_b} - m_{\Lambda^*})}{\sqrt{q^2}} \frac{s_+\sqrt{s_-}}{\sqrt{6} m_{\Lambda^*}} (C_L - C_R) \quad ({\rm A7})$$

$$A^L_{\perp_1} = -2\sqrt{2} N f_\perp^V \frac{s_-\sqrt{s_+}}{\sqrt{3} m_{\Lambda^*}} (C_L + C_R) \quad ({\rm A8})$$

$$A^L_{\parallel_1} = -2\sqrt{2} N \left(f_\perp^A \frac{s_+\sqrt{s_-}}{\sqrt{3} m_{\Lambda^*}} (C_L - C_R) \right), \quad ({\rm A9})$$

$$A^{L(R)}_{\perp_t} = \mp\sqrt{2} N f_t^V \frac{(m_{\Lambda_b} - m_{\Lambda^*})}{\sqrt{q^2}} \frac{s_+\sqrt{s_-}}{\sqrt{6} m_{\Lambda^*}} (-C_L - C_R), \quad ({\rm A10})$$

$$A^{L(R)}_{\parallel_t} = \pm\sqrt{2} N f_t^A \frac{(m_{\Lambda_b} + m_{\Lambda^*})}{\sqrt{q^2}} \frac{s_-\sqrt{s_+}}{\sqrt{6} m_{\Lambda^*}} (-C_L + C_R), \quad ({\rm A11})$$

where

$$N = G_F V_{tb} V_{ts}^* \alpha_e \sqrt{\tau_{\Lambda_b} \frac{q^2 \sqrt{\lambda(m^2_{\Lambda_b}, m^2_{\Lambda^*}, q^2)}}{3 \times 2^{11} m^3_{\Lambda_b} \pi^5} \mathcal{B}_{\Lambda^*}}, \quad ({\rm A12})$$

and $B^R_{\perp_1}, B^R_{\parallel_1}, A^R_{\perp_0}, A^R_{\parallel_0}, A^R_{\perp_1}, A^R_{\parallel_1} = 0$.

Similarly for the $\Lambda_b \to \Lambda(\to p\pi)\nu\bar{\nu}$ decay, the transversity amplitudes can be defined as

$$A^L_{\perp_1} = -2\sqrt{2} N f_\perp^V \sqrt{2 s_-} (C_L + C_R), \quad ({\rm A13})$$

$$A^L_{\parallel_1} = 2\sqrt{2} N f_\perp^A \sqrt{2 s_+} (C_L - C_R), \quad ({\rm A14})$$

$$A^L_{\perp_0} = 2\sqrt{2} N f_0^V (m_{\Lambda_b} + m_{\Lambda^*}) \sqrt{\frac{s_-}{q^2}} (C_L + C_R), \quad ({\rm A15})$$

$$A^L_{\parallel_0} = -2\sqrt{2} N f_0^A (m_{\Lambda_b} - m_{\Lambda^*}) \sqrt{\frac{s_+}{q^2}} (C_L - C_R), \quad ({\rm A16})$$

$$A_{\perp t} = 2\sqrt{2} N f_t^V (m_{\Lambda_b} - m_{\Lambda^*}) \sqrt{\frac{s_+}{q^2}} C_L, \quad ({\rm A17})$$

$$A_{\parallel t} = -2\sqrt{2} N f_t^A (m_{\Lambda_b} + m_{\Lambda^*}) \sqrt{\frac{s_-}{q^2}} C_L. \quad ({\rm A18})$$

Here $A^R_{\perp_1}, A^R_{\parallel_1}, A^R_{\perp_0}, A^R_{\parallel_0} = 0$ and

$$N(q^2) = G_F V_{tb} V_{ts}^* \alpha_e \sqrt{\tau_{\Lambda_b} \frac{q^2 \sqrt{\lambda(m^2_{\Lambda_b}, m^2_{\Lambda}, q^2)}}{3.2^{11} m^3_{\Lambda_b} \pi^5} \mathcal{B}_{\Lambda}}. \quad ({\rm A19})$$

[1] R. Aaij *et al.*, Test of lepton universality in beauty-quark decays, Nat. Phys. **18**, 277 (2022).
[2] R. Aaij *et al.*, Test of lepton universality with $B^0 \to K^{*0}\ell^+\ell^-$ decays, J. High Energy Phys. 08 (2017) 055.
[3] R. Aaij *et al.*, Measurement of CP-averaged observables in the $B^0 \to K^{*0}\mu^+\mu^-$ decay, Phys. Rev. Lett. **125**, 011802 (2020).
[4] A. Abdesselam *et al.*, Test of lepton-flavor universality in $B \to K^*\ell^+\ell^-$ decays at Belle, Phys. Rev. Lett. **126**, 161801 (2021).
[5] M. Bordone, G. Isidori, and A. Pattori, On the standard model predictions for R_K and R_{K^*}, Eur. Phys. J. C **76**, 440 (2016).
[6] G. Hiller and F. Kruger, More model-independent analysis of $b \to s$ processes, Phys. Rev. D **69**, 074020 (2004).
[7] R. Aaij *et al.* (LHCb Collaboration), Test of lepton universality in $b \to s\ell^+\ell^-$ decays, Phys. Rev. Lett. **131**, 051803 (2023).
[8] R. Aaij *et al.* (LHCb Collaboration), Measurement of lepton universality parameters in $B^+ \to K^+\ell^+\ell^-$ and $B^0 \to K^{*0}\ell^+\ell^-$ decays, Phys. Rev. D **108**, 032002 (2023).
[9] R. Aaij *et al.*, Measurement of form-factor-independent observables in the decay $B^0 \to K^{*0}\mu^+\mu^-$, Phys. Rev. Lett. **111**, 191801 (2013).
[10] R. Aaij *et al.*, Angular analysis of the $B^0 \to K^{*0}\mu^+\mu^-$ decay using 3 fb^{-1} of integrated luminosity, J. High Energy Phys. 02 (2016) 104.
[11] M. Aaboud *et al.*, Angular analysis of $B_d^0 \to K^*\mu^+\mu^-$ decays in pp collisions at $\sqrt{s} = 8$ TeV with the ATLAS detector, J. High Energy Phys. 10 (2018) 047.
[12] A. M. Sirunyan *et al.* (CMS Collaboration), Measurement of the P_1 and P_5' angular parameters of the decay $B \to K^*\mu^+\mu^-$ in proton proton collisions at $\sqrt{s} = 8$ TeV, Phys. Lett. B **781**, 517 (2018).
[13] A. Abdesselam *et al.* (Belle Collaboration), Angular analysis of $B^0 \to K^*(892)^0\ell^+\ell^-$, in *Proceedings of LHCSki 2016—A First Discussion of 13 TeV Results : Obergurgl, Austria, April 10–15, 2016 Contribution to: LHC Ski 2016*, Report No.: BELLE-CONF-1603 (2016).
[14] S. Descotes-Genon, J. Matias, M. Ramon, and J. Virto, Implications from clean observables for the binned analysis of $B \to K*\mu^+\mu^-$ at large recoil, J. High Energy Phys. 01 (2013) 048.
[15] S. Descotes-Genon, T. Hurth, J. Matias, and J. Virto, Optimizing the basis of $B \to K^*ll$ observables in the full kinematic range, J. High Energy Phys. 05 (2013) 137.
[16] S. Descotes-Genon, L. Hofer, J. Matias, and J. Virto, On the impact of power corrections in the prediction of $B \to K^*\mu^+\mu^-$ observables, J. High Energy Phys. 12 (2014) 125.
[17] R. Aaij *et al.*, Branching fraction measurements of the rare $B_s^0 \to \phi\mu^+\mu^-$ and $B_s^0 \to f_2'(1525)\mu^+\mu^-$- decays, Phys. Rev. Lett. **127**, 151801 (2021).
[18] R. Aaij *et al.*, Differential branching fraction and angular analysis of the decay $B_s^0 \to \phi\mu^+\mu^-$, J. High Energy Phys. 07 (2013) 084.
[19] R. Aaij *et al.*, Angular analysis and differential branching fraction of the decay $B_s^0 \to \phi\mu^+\mu^-$, J. High Energy Phys. 09 (2015) 179.
[20] R. Aaij *et al.*, Tests of lepton universality using $B^0 \to K_S^0\ell^+\ell^-$ and $B^+ \to K^{*+}\ell^+\ell^-$ decays, Phys. Rev. Lett. **128**, 191802 (2022).
[21] F. Dattola (Belle-II Collaboration), Search for $B^+ \to K^+\nu\bar{\nu}$ decays with an inclusive tagging method at the Belle II experiment, arXiv:2105.05754.
[22] N. Rajeev and R. Dutta, Consequences of $\mathrm{b} \to s\mu^+\mu^-$ anomalies on $\mathrm{B} \to \mathrm{K}(*)\nu\nu^-$, $\mathrm{Bs} \to (\eta, \eta')\nu\nu^-$ and $\mathrm{Bs} \to \phi\nu\nu^-$ decay observables, Phys. Rev. D **105**, 115028 (2022).
[23] M. K. Mohapatra, N. Rajeev, and R. Dutta, Combined analysis of $\mathrm{Bc} \to \mathrm{Ds}(*)\mu^+\mu^-$ and $\mathrm{Bc} \to \mathrm{Ds}(*)\nu\nu^-$ decays within Z' and leptoquark new physics models, Phys. Rev. D **105**, 115022 (2022).
[24] Y. Li, J. Hua, and K.-C. Yang, $B \to K1\ell^+\ell^-$ Decays in a family non-universal Z' model, Eur. Phys. J. C **71**, 1775 (2011).
[25] Z.-R. Huang, M. A. Paracha, I. Ahmed, and C.-D. Lü, Testing leptoquark and Z' models via $B \to K_1(1270, 1400)\mu^+\mu^-$ decays, Phys. Rev. D **100**, 055038 (2019).
[26] F. Falahati and A. Zahedidareshouri, Forward-backward asymmetries of $\bar{B} \to \bar{K}_1(1270)\ell^+\ell^-$ and $\bar{B} \to \bar{K}^*\ell^+\ell^-$ transitions in two Higgs doublet model, Phys. Rev. D **90**, 075002 (2014).
[27] I. Ahmed, M. Ali Paracha, and M. J. Aslam, Model independent analysis of the forward-backward asymmetry for the $B \to K_1\mu^+\mu^-$ decay, Eur. Phys. J. C **71**, 1521 (2011).
[28] B. Capdevila, A. Crivellin, S. Descotes-Genon, J. Matias, and J. Virto, Patterns of new physics in $b \to s\ell^+\ell^-$ transitions in the light of recent data, J. High Energy Phys. 01 (2018) 093.
[29] V. Bashiry, Lepton polarization in $B \to K_1\ell^+\ell^-$ decays, J. High Energy Phys. 06 (2009) 062.
[30] W.-F. Wang and Z.-J. Xiao, The semileptonic decays $B/B_s \to (\pi, K)(\ell^+\ell^-, \ell\nu, \nu\bar{\nu})$ in the perturbative QCD approach beyond the leading-order, Phys. Rev. D **86**, 114025 (2012).
[31] R.-H. Li, C.-D. Lu, and W. Wang, Branching ratios, forward-backward asymmetries and angular distributions of $B \to K_2^* l^+ l^-$ in the standard model and new physics scenarios, Phys. Rev. D **83**, 034034 (2011).
[32] N. Rajeev, N. Sahoo, and R. Dutta, Angular analysis of $B_s \to f_2'(1525)(\to K^+K^-)\mu^+\mu^-$ decays as a probe to lepton flavor universality violation, Phys. Rev. D **103**, 095007 (2021).
[33] T. E. Browder, N. G. Deshpande, R. Mandal, and R. Sinha, Impact of $B \to K\nu\bar{\nu}$ measurements on beyond the standard model theories, Phys. Rev. D **104**, 053007 (2021).
[34] C. Bobeth, A. J. Buras, F. Kruger, and J. Urban, QCD corrections to $\bar{B} \to X_{d,s}\nu\bar{\nu}$, $\bar{B}_{d,s} \to \ell^+\ell^-$, $K \to \pi\nu\bar{\nu}$ and $K_L \to \mu^+\mu^-$ in the MSSM, Nucl. Phys. **B630**, 87 (2002).
[35] W. Altmannshofer, A. J. Buras, D. M. Straub, and M. Wick, New strategies for new physics search in $B \to K^*\nu\bar{\nu}$, $B \to K\nu\bar{\nu}$ and $B \to X_s\nu\bar{\nu}$ decays, J. High Energy Phys. 04 (2009) 022.
[36] S. Descotes-Genon, S. Fajfer, J. F. Kamenik, and M. Novoa-Brunet, Implications of $b \to s\mu\mu$ anomalies for future measurements of $B \to K^{(*)}\nu\bar{\nu}$ and $K \to \pi\nu\bar{\nu}$, Phys. Lett. B **809**, 135769 (2020).

[37] S. Fajfer, N. Košnik, and L. Vale Silva, Footprints of leptoquarks: From $R_{K^{(*)}}$ to $K \to \pi\nu\bar{\nu}$, Eur. Phys. J. C **78**, 275 (2018).

[38] N. R. Singh Chundawat, New physics in $B \to K^*\tau^+\tau^-$: A model independent analysis, Phys. Rev. D **107**, 055004 (2023).

[39] N. R. Singh Chundawat, CP violation in $b \to s\ell\ell$: A model independent analysis, Phys. Rev. D **107**, 075014 (2023).

[40] N. Gubernari, M. Reboud, D. van Dyk, and J. Virto, Improved theory predictions and global analysis of exclusive $b \to s\mu^+\mu^-$ processes, J. High Energy Phys. 09 (2022) 133.

[41] R. Aaij *et al.*, Test of lepton universality with $\Lambda_b^0 \to pK^-\ell^+\ell^-$ decays, J. High Energy Phys. 05 (2020) 040.

[42] S. Meinel and G. Rendon, $\Lambda_b \to \Lambda^*(1520)\ell^+\ell^-$ form factors from lattice QCD, Phys. Rev. D **103**, 074505 (2021).

[43] S. Meinel and G. Rendon, $\Lambda_c \to \Lambda^*(1520)$ form factors from lattice QCD and improved analysis of the $\Lambda_b \to \Lambda^*(1520)$ and $\Lambda_b \to \Lambda c*(2595, 2625)$ form factors, Phys. Rev. D **105**, 054511 (2022).

[44] S. Descotes-Genon and M. Novoa-Brunet, Angular analysis of the rare decay $\Lambda_b \to \Lambda(1520)(\to NK)\ell^+\ell^-$, J. High Energy Phys. 06 (2019) 136; 06 (2020) 102(E).

[45] D. Das and J. Das, The $\Lambda_b \to \Lambda^*(1520)(\to N\bar{K})\ell^+\ell^-$ decay at low-recoil in HQET, J. High Energy Phys. 07 (2020) 002.

[46] Y. Amhis, S. Descotes-Genon, C. Marin Benito, M. Novoa-Brunet, and M.-H. Schune, Prospects for new physics searches with $\Lambda_b^0 \to \Lambda(1520)\ell^+\ell^-$ decays, Eur. Phys. J. Plus **136**, 614 (2021).

[47] Y.-S. Li, S.-P. Jin, J. Gao, and X. Liu, The transition form factors and angular distributions of the $\boldsymbol{\Lambda_b \to \Lambda(1520)}(\to \boldsymbol{N\bar{K}})\ell^+\ell^-$ decay supported by baryon spectroscopy, Phys. Rev. D **107**, 093003 (2023).

[48] W. Detmold, C. J. D. Lin, S. Meinel, and M. Wingate, $\Lambda_b\Lambda\ell^+\ell^-$ form factors and differential branching fraction from lattice QCD, Phys. Rev. D **87**, 074502 (2013).

[49] W. Detmold and S. Meinel, $\Lambda_b \to \Lambda\ell^+\ell^-$ form factors, differential branching fraction, and angular observables from lattice QCD with relativistic b quarks, Phys. Rev. D **93**, 074501 (2016).

[50] C.-H. Chen and C. Q. Geng, Lepton asymmetries in heavy baryon decays of $\Lambda_b \to \Lambda l^+l^-$, Phys. Lett. B **516**, 327 (2001).

[51] M. J. Aslam, Y.-M. Wang, and C.-D. Lu, Exclusive semileptonic decays of $\Lambda_b \to \Lambda l^+l^-$ in supersymmetric theories, Phys. Rev. D **78**, 114032 (2008).

[52] Y.-m. Wang, Y. Li, and C.-D. Lu, Rare decays of $\Lambda_b \to \Lambda + \gamma$ and $\Lambda_b \to \Lambda + l^+l^-$ in the light-cone sum rules, Eur. Phys. J. C **59**, 861 (2009).

[53] Y.-M. Wang, Y.-L. Shen, and C.-D. Lu, $\Lambda_b \to p$, Λ transition form factors from QCD light-cone sum rules, Phys. Rev. D **80**, 074012 (2009).

[54] T. M. Aliev, K. Azizi, and M. Savci, Analysis of the $\Lambda_b \to \Lambda\ell^+\ell^-$ decay in QCD, Phys. Rev. D **81**, 056006 (2010).

[55] Y.-M. Wang and Y.-L. Shen, Perturbative corrections to $\Lambda_b \to \Lambda$ form factors from QCD light-cone sum rules, J. High Energy Phys. 02 (2016) 179.

[56] T. Gutsche, M. A. Ivanov, J. G. Korner, V. E. Lyubovitskij, and P. Santorelli, Rare baryon decays $\Lambda_b \to \Lambda l^+l^-(l = e, \mu, \tau)$ and $\Lambda_b \to \Lambda\gamma$: Differential and total rates, lepton- and hadron-side forward-backward asymmetries, Phys. Rev. D **87**, 074031 (2013).

[57] L. Mott and W. Roberts, Rare dileptonic decays of Λ_b in a quark model, Int. J. Mod. Phys. A **27**, 1250016 (2012).

[58] L.-L. Liu, X.-W. Kang, Z.-Y. Wang, and X.-H. Guo, Rare $\Lambda_b \to \Lambda\ell^+\ell^-$ decay in the Bethe-Salpeter equation approach, Chin. Phys. C **44**, 083107 (2020).

[59] T. Aaltonen *et al.*, Observation of the baryonic flavor-changing neutral current decay $\Lambda_b \to \Lambda\mu^+\mu^-$, Phys. Rev. Lett. **107**, 201802 (2011).

[60] R. Aaij *et al.*, Differential branching fraction and angular analysis of $\Lambda_b^0 \to \Lambda\mu^+\mu^-$ decays, J. High Energy Phys. 06 (2015) 115; 09 (2018) 145(E).

[61] R. Aaij *et al.*, Angular moments of the decay $\Lambda_b^0 \to \Lambda\mu^+\mu^-$ at low hadronic recoil, J. High Energy Phys. 09 (2018) 146.

[62] C.-S. Huang and H.-G. Yan, Exclusive rare decays of heavy baryons to light baryons: $\Lambda_b \to \Lambda\gamma$ and $\Lambda_b \to \Lambda l^+l^-$, Phys. Rev. D **59**, 114022 (1999); **61**, 039901(E) (2000).

[63] T. Feldmann and M. W. Y. Yip, Form factors for $\Lambda_b \to \Lambda$ transitions in the soft-collinear effective theory, Phys. Rev. D **85**, 014035 (2012); **86**, 079901(E) (2012).

[64] A. Ali, C. Hambrock, A. Y. Parkhomenko, and W. Wang, Light-cone distribution amplitudes of the ground state bottom baryons in HQET, Eur. Phys. J. C **73**, 2302 (2013).

[65] G. Bell, T. Feldmann, Y.-M. Wang, and M. W. Y. Yip, Light-cone distribution amplitudes for heavy-quark hadrons, J. High Energy Phys. 11 (2013) 191.

[66] V. M. Braun, S. E. Derkachov, and A. N. Manashov, Integrability of the evolution equations for heavy–light baryon distribution amplitudes, Phys. Lett. B **738**, 334 (2014).

[67] D. Das, Model independent new physics analysis in $\Lambda_b \to \Lambda\mu^+\mu^-$ decay, Eur. Phys. J. C **78**, 230 (2018).

[68] D. Das, On the angular distribution of $\Lambda_b \to \Lambda(\to N\pi)\tau^+\tau^-$ decay, J. High Energy Phys. 07 (2018) 063.

[69] S. Roy, R. Sain, and R. Sinha, Lepton mass effects and angular observables in $\Lambda_b \to \Lambda(\to p\pi)\ell^+\ell^-$, Phys. Rev. D **96**, 116005 (2017).

[70] H. Yan, Angular distribution of the rare decay $\Lambda_b \to \Lambda (\to N\pi)\ell^+\ell^-$, arXiv:1911.11568.

[71] P. Böer, T. Feldmann, and D. van Dyk, Angular analysis of the decay $\Lambda_b \to \Lambda(\to N\pi)\ell^+\ell^-$, J. High Energy Phys. 01 (2015) 155.

[72] T. Blake and M. Kreps, Angular distribution of polarised Λ_b baryons decaying to $\Lambda\ell^+\ell^-$, J. High Energy Phys. 11 (2017) 138.

[73] T. Blake, S. Meinel, and D. van Dyk, Bayesian analysis of $b \to s\mu^+\mu^-$ Wilson coefficients using the full angular distribution of $\Lambda_b \to \Lambda(\to p\pi^-)\mu^+\mu^-$ decays, Phys. Rev. D **101**, 035023 (2020).

[74] C.-H. Chen and C. Q. Geng, Study of $\Lambda_b \to \Lambda$ neutrino anti-neutrino with polarized baryons, Phys. Rev. D **63**, 054005 (2001).

[75] B. B. Sirvanli, Semileptonic $\Lambda_b \to \Lambda$ neutrino anti-neutrino decay in the leptophobic Z-prime model, Mod. Phys. Lett. A **23**, 347 (2008).

[76] B. Grzadkowski, M. Iskrzynski, M. Misiak, and J. Rosiek, Dimension-six terms in the standard model Lagrangian, J. High Energy Phys. 10 (2010) 085.

[77] A. J. Buras, J. Girrbach-Noe, C. Niehoff, and D. M. Straub, $B \to K^{(*)}\nu\bar{\nu}$ decays in the standard model and beyond, J. High Energy Phys. 02 (2015) 184.

[78] A. Khodjamirian, T. Mannel, A. A. Pivovarov, and Y. M. Wang, Charm-loop effect in $B \to K^{(*)}\ell^+\ell^-$ and $B \to K^*\gamma$, J. High Energy Phys. 09 (2010) 089.

[79] A. Khodjamirian, T. Mannel, and Y. M. Wang, $B \to K\ell^+\ell^-$ decay at large hadronic recoil, J. High Energy Phys. 02 (2013) 010.

[80] C. Bobeth, M. Chrzaszcz, D. van Dyk, and J. Virto, Long-distance effects in $B \to K^*\ell\ell$ from analyticity, Eur. Phys. J. C **78**, 451 (2018).

[81] N. Gubernari, D. van Dyk, and J. Virto, Non-local matrix elements in $B_{(s)} \to \{K^{(*)}, \phi\}\ell^+\ell^-$, J. High Energy Phys. 02 (2021) 088.

[82] R. L. Workman *et al.*, Review of particle physics, Prog. Theor. Exp. Phys. **2022**, 083C01 (2022).

[83] R. Aleksan, L. Oliver, and E. Perez, Study of *CP* violation in $B^\pm$ decays to $\overline{D^0}(D^0)K^\pm$ at FCCee, arXiv:2107.05311.

[84] W. Altmannshofer *et al.*, The Belle II physics book, Prog. Theor. Exp. Phys. **2019**, 123C01 (2019). **2020**, 029201(E) (2020).

[85] Y. Amhis, M. Hartmann, C. Helsens, D. Hill, and O. Sumensari, Prospects for $B_c^+ \to \tau^+ \nu$ at FCC-ee, J. High Energy Phys. 12 (2021) 133.

[86] Y. Amhis, M. Kenzie, M. Reboud, and A. R. Wiederhold, Prospects for searches of $b \to s\nu\bar{\nu}$ decays at FCC-ee, arXiv:2309.11353.

[87] R. Aaij *et al.*, Search for lepton-universality violation in $B^+ \to K^+\ell^+\ell^-$ decays, Phys. Rev. Lett. **122**, 191801 (2019).

[88] A. M. Sirunyan *et al.*, Measurement of angular parameters from the decay $B^0 \to K^{*0}\mu^+\mu^-$ in proton-proton collisions at $\sqrt{s} = 8$ TeV, Phys. Lett. B **781**, 517 (2018).

[89] R. Aaij *et al.*, Analysis of neutral B-meson decays into two muons, Phys. Rev. Lett. **128**, 041801 (2022).

[90] J. Grygier *et al.*, Search for $\boldsymbol{B \to h\nu\bar{\nu}}$ decays with semi-leptonic tagging at Belle, Phys. Rev. D **96**, 091101 (2017); **97**, 099902(A) (2018).